

# Molecular Self-Assembly at Bare Semiconductor Surfaces: Characterization of a Homologous Series of *n*-Alkanethiolate Monolayers on GaAs(001)

Christine L. McGuiness,<sup>†</sup> Daniel Blasini,<sup>‡</sup> John P. Masejewski,<sup>†,‡</sup> Sundararajan Uppili,<sup>†,||</sup> Orlando M. Cabarcos,<sup>†</sup> Detlef Smilgies,<sup>§</sup> and David L. Allara<sup>†,\*</sup>

<sup>†</sup>Departments of Chemistry and Materials Science, The Pennsylvania State University, 104 Chemistry Building, University Park, Pennsylvania 16801-6300, <sup>‡</sup>Department of Chemistry, Cornell University, Baker Laboratory, Ithaca, New York 14853-1301, and <sup>§</sup>Cornell High Energy Synchrotron Source, 200L Wilson Lab, Ithaca, New York 14853.

<sup>||</sup>Present address: Department of Chemistry, The University of Pittsburgh, Pittsburgh, PA 15260. <sup>||</sup>Present address: Conoco Phillips, Bartlesville, OK 74004.

**ABSTRACT** Structural trends for a homologous series of *n*-alkanethiolate self-assembled monolayers (SAMs),  $C_nH_{2n+1}S-$  with  $12 \leq n \leq 19$ , on GaAs(001), studied by a combination of grazing incidence X-ray diffraction and infrared spectroscopy, along with ancillary probes, show an overall decay in organization with decreasing *n*, with the largest changes occurring below  $n = 15-16$ . The long-chain monolayers form a mosaic structure with  $\leq 10$  nm domains of molecules organized in an incommensurate pseudo-hcp arrangement with nearest neighbor distances of 4.70 and 5.02 Å, a 21.2 Å<sup>2</sup> area per chain, two chains per subcell in a herringbone packing with a chain tilt angle of 14°, and preferential domain alignment along the substrate  $[1\bar{1}0]([110])$  step edge direction. In contrast, for  $n < 14$  no evidence of translational ordering is seen and the alkyl chains exhibit a loss of conformational ordering and coverage relative to the  $n > 16$  cases. A 4'-methyl-biphenyl-4-thiolate companion SAM shows evidence for ordered structures but with lattice parameters close to those expected for a structure commensurate with the intrinsic GaAs(001) square lattice. These trends are explained on the basis of competitions between lattice, interfacial, and intermolecular forces controlling the nanoscale structures of the SAMs. Overall these results provide an important aspect of understanding the effects of SAM formation on surface properties such as electronic and chemical passivation.

**KEYWORDS:** self-assembled monolayers · adsorbate ordering · GaAs(001) · infrared spectroscopy · grazing incidence X-ray diffraction · X-ray photoelectron spectroscopy · contact angle

The formation of ordered, densely packed self-assembled monolayers (SAMs) on metal and semiconductor surfaces has been of longstanding interest.<sup>1,2</sup> The assembly process is mediated by the interplay of molecule–substrate attachment, molecule–molecule packing, and SAM–ambient interface energetics. Attachment chemistries range across Brønsted acid–base interactions (e.g., RCOOH to the native oxide surfaces of Al and Ag<sup>3,4</sup>), adsorbed water mediation (e.g., Langmuir-type SAMs with  $RSiO_xH_y$  to  $SiO_2^{5-7}$ ), and covalent–polar interactions (e.g., RSH to Au,<sup>8,9</sup> Ag,<sup>2,10</sup> or GaAs<sup>11,12</sup>). In general, the most incisive studies of assembly structures

have been for simple linear chain aliphatic adsorbates, which involve stabilization by alkyl chain intermolecular interactions.

Monolayers prepared from alkanethiols are the most widely studied example, and structures have been characterized for SAMs on both metal surfaces, including Au,<sup>10,13</sup> Ag,<sup>2,10</sup> Cu,<sup>10</sup> Pd,<sup>14</sup> and Pt,<sup>15</sup> and semiconductor surfaces, including GaAs,<sup>11</sup> InP,<sup>16–19</sup> and InAs.<sup>20</sup> Though well-organized alkyl-type SAMs on these substrates all exhibit dense packing with highly hydrophobic and oleophobic wetting responses, fundamental differences in surface chemistry can impose distinct structural differences in coverage, packing symmetry, molecular tilt angle, bonding geometry, and odd-even chain length effects. For example, alkanethiolate SAMs formed on Au{111} and Ag{111} have different lattice structures: a  $(\sqrt{3} \times \sqrt{3})R30^\circ$  superlattice with a  $\sim 26-30^\circ$  molecular tilt angle for Au{111}<sup>2,21–25</sup> and an incommensurate superlattice with a  $\sim 10^\circ$  molecular tilt angle for Ag<sup>2,10,26,27</sup>. The detailed understanding of the complexities of SAM structures is best known for the cases of alkanethiolates on noble metal surfaces, due in good part to careful, systematic development of structural trends for homologous series of different length alkanethiols where molecule–substrate bonding can be kept nearly invariant and changes in film properties can be interpreted primarily in terms of chain–chain interaction effects.<sup>10,13–15,25,28–32</sup> This understanding has been broadly important in guiding developments in a number of applications including corrosion resistance,

\*Address correspondence to dla3@psu.edu.

Received for review June 5, 2007 and accepted July 16, 2007.

Published online August 14, 2007.  
10.1021/nn7000596 CCC: \$37.00

© 2007 American Chemical Society

molecular electronic devices, and nanolithography, which all involve the ability to construct densely packed arrays with minimal defect densities.<sup>33,34</sup>

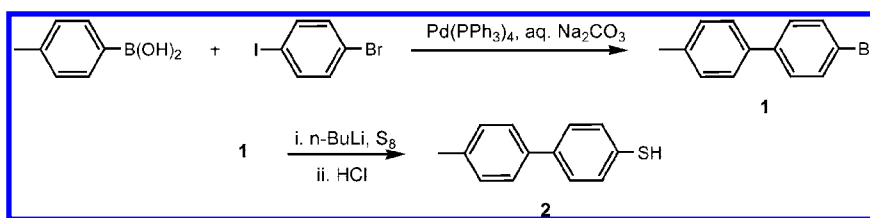
In the case of alkanethiolate monolayers on semiconductor substrates, there have been almost no systematic studies of structure, despite the technological importance of these materials. This is most notable for GaAs, which is widely used for electronics and optoelectronics devices<sup>35–37</sup> and for which densely packed SAMs can be formed. In a previous report,<sup>12</sup> a combination of infrared spectroscopy (IRS), near edge X-ray absorption fine structure (NEXAFS), liquid drop contact angle, and X-ray photoelectron spectroscopy (XPS) measurements were used to conclude that octadecanethiolate (**C<sub>18</sub>**) SAMs on GaAs(001) can be well-organized with a high degree of chain conformational ordering, direct S–(GaAs) bonding, and a  $\sim 14^\circ$  tilt from the surface normal. Of particular note was the implication from the data that the average spacings between the molecules did not fit with the intrinsic (001) substrate square lattice spacings; thus the adsorbate bonding sites would have to be incommensurate with the intrinsic substrate lattice. Comparison of this conclusion with the earlier reports of the formation of commensurate overlayer structures from chemisorption of simple inorganic sulfide species on GaAs(001)<sup>38–43</sup> shows that the alkyl chains in the alkanethiolates must exert significant influence on their monolayer structure. In our earlier report<sup>44</sup> it was also observed that the short chain **C<sub>12</sub>** SAM appeared much more disorganized with lower coverages, implying that the existing substrate bonding site distributions were unfavorable for uniform adsorbate packing and the diminished chain–chain interactions were not sufficient to force the chains into a high degree of organization. Clearly, gaining an accurate understanding of the basis for these effects would benefit greatly from a rigorous, systematic study with a homologous series of *n*-alkanethiols.

Recently, there have been two reports of comparisons of the characteristics of monolayers from different length alkanethiolates on GaAs(001) surfaces.<sup>45,46</sup> Jun and co-workers, in a study of the electrical passivation of alkanethiolates SAMs, have reported thickness trends for a homologous series of even chain length *n*-alkanethiolate and dithiolate SAMs on GaAs(001) in which the thickness values were deduced from XPS and single wavelength ellipsometry (SWE) data.<sup>45</sup> From both analytical methods, the SAMs were concluded to exhibit a  $\sim 60^\circ$  molecular tilt, similar to the value in the first report of alkanethiolates SAMs on GaAs(001),<sup>11,47</sup> but conflicting significantly with a more recent, rigorously derived value of  $14 \pm 1^\circ$  for a highly organized **C<sub>18</sub>** SAM.<sup>12</sup> Jun and co-workers also noted a “clear break”<sup>45</sup> in their observed linear behavior in the thickness–

chain length dependence data at  $n = 14$  (for  $C_nH_{2n+1}S^-$ ). Nesher and co-workers, in a study of the electrical characteristics of GaAs–(001) *n*-alkanethiolate–Hg junctions for alkyl chains with  $n = 12, 14, 15$ , and  $18$ ,<sup>46,48</sup> characterized the SAMs by XPS-derived thicknesses, contact angles, and IRS-derived estimates of the relative extent of chain conformational ordering. For the case of the **C<sub>18</sub>** SAM they concluded that the chains were densely packed and oriented nearly perpendicular to the surface, in agreement with our earlier report,<sup>12</sup> but did not show any evidence for any distinct break in the structure–chain length trends. Overall, although these studies provide some useful qualitative information of the SAM structures, it is problematic to extract any details of the existence of translational ordering of the SAM adsorbate molecules or quantitative evidence for specific chain structure characteristics such as tilt angles.

Recognizing the important gaps in the structural aspects of alkanethiolate SAMs on GaAs (001) surfaces, we have continued our investigations to include a homologous series of these SAMs formed from our earlier developed, highly controlled preparation methods for organized monolayers.<sup>12</sup> Our approach involves the use of multiple, quantitative surface probes coupled with rigorous data interpretation. In this paper we report structural and surface wetting trends for a series of monolayers assembled from  $C_nH_{2n+1}SH$  with  $12 \leq n \leq 19$ . In addition, an aromatic molecule SAM terminated by a  $CH_3$  group was prepared from 4'-methyl-biphenyl-4-thiol (MBT, structure **2** in Scheme 1) and studied in detail for comparison with the aliphatic hydrocarbon cases to better understand the contributing factors that drive self-assembly on GaAs(001) surfaces. MBT was chosen for comparison because it is a homologue of other phenyl systems that have been investigated on metal surfaces,<sup>49,50</sup> has shown to assemble on GaAs(001) surfaces,<sup>51–54</sup> and also has strong IR intensities, an important factor for obtaining unambiguous IRS spectra on low reflectivity surfaces. Because of the inability of scanning tunneling microscopy to probe the thicker, long-chain alkanethiolate SAMs and the difficulty of applying high precision atomic force microscopy to these substrates,<sup>12</sup> we chose grazing incidence X-ray diffraction (GIXRD) as the primary probe for characterizing surface ordering.

From combined IRS and GIXRD results we establish for the first time the presence of translationally ordered



Scheme 1. Reaction scheme for the 4'-methyl-biphenyl-4-thiol molecule.

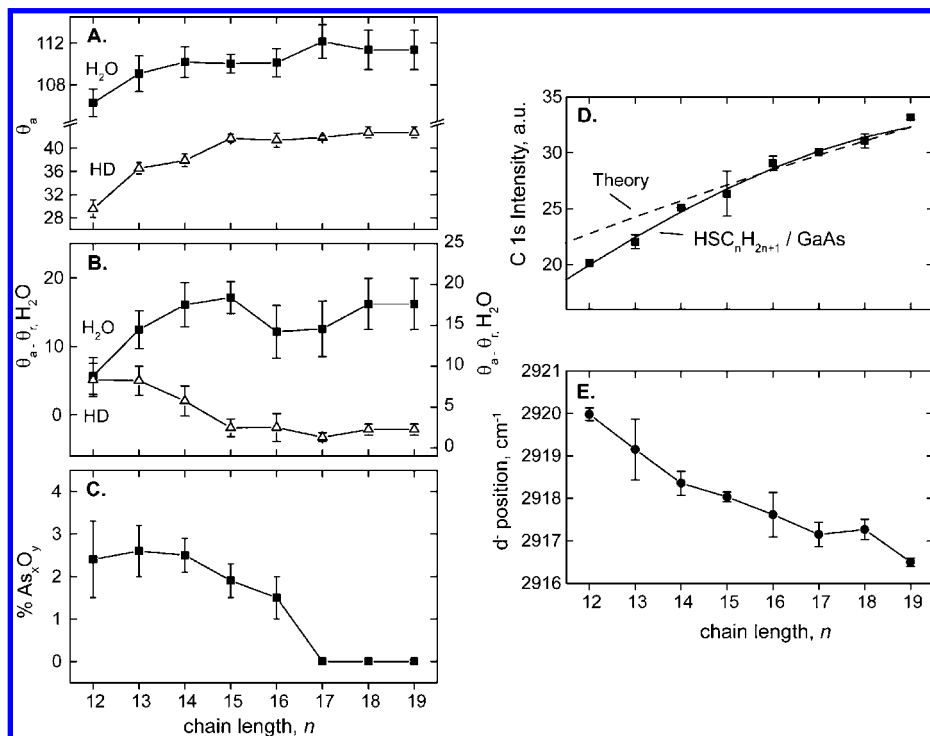


**Figure 1.** Alkanethiolate,  $C_nH_{2n+1}S^-$ , monolayer characteristics on GaAs(001) as a function of chain length,  $n$ . (A) Advancing contact angle  $\theta_a$  of H<sub>2</sub>O and hexadecane (HD). (B) Associated hysteresis ( $\theta_a - \theta_r$ ) for H<sub>2</sub>O and HD contact angles. (C) Percent As<sub>x</sub>O<sub>y</sub> from the total XPS As 3d signal (for  $n > 16$  no As<sub>x</sub>O<sub>y</sub> signals were detected within the noise limit). (D) XPS C 1s intensity, where the solid line is a guide to the eye for the experimental data and the dashed line is the theoretical dependence based on a constant monolayer coverage and film density for all values of  $n$  and referenced to the intensity of the C<sub>18</sub> SAM. (E) d<sup>-</sup> mode IR peak position. See text for details.

arrangements of the adsorbate molecules in the aliphatic SAMs. From ancillary XPS and contact angle measurements we conclude that there is a gradual decrease, as opposed to an abrupt change, in SAM thickness, coverage, and surface organization with decreasing chain length with apparent limiting coverages and surface organization for  $n \geq 16$ . Extensive GIXRD data acquired for the case of the C<sub>18</sub> SAM definitively show the presence of a mosaic structure with  $\leq 10$  nm domains with molecules arranged in a rhombohedral or pseudo hexagonal close-packed (pseudo-hcp) unit cell structure, oriented along the  $[1\bar{1}0]([110])$  direction but incommensurate with the underlying bulk GaAs(001) lattice substrate. The IRS measurements also show a subtle odd–even chain length dependence of the C–H stretching modes that can be understood by the presence of two types of chains in the unit cell differing by a  $\sim 90^\circ$  (setting angle) twist angle around the long-chain axis, consistent with a highly dense crystalline packing of the hydrocarbon chains.<sup>10</sup> For  $n \leq 14$  the SAMs fail to show any diffraction pattern and the IRS data indicate a significant decrease in the conformational ordering of the chains. Finally, the MBT molecule forms a mosaic structure of ordered, oriented domains as evidenced by a weak diffraction pattern but with larger molecule spacings than for the alkanethiolate SAMs. Overall our data on both types of SAMs are consistent with inter-

molecular interactions acting as driving forces capable of inducing short range restructuring of the intrinsic (001) surface lattice.

## RESULTS

**Surface Organization from Contact Angle Measurements.** For each monolayer, the advancing angle of a sessile drop ( $\theta_a$ ) was measured for H<sub>2</sub>O and HD probe liquids. These values and the resulting hysteresis ( $\theta_a - \theta_r$ ) are reported in Figure 1A and B.

For both H<sub>2</sub>O and HD,  $\theta_a$  increases nearly monotonically with chain length and reaches maximum values of  $111 \pm 3^\circ$  and  $43 \pm 1^\circ$ , respectively, close to the values obtained in other well-formed alkane SAMs, e.g.,  $\sim 110$ – $115^\circ$  [ $(\theta_a - \theta_r) \sim 10^\circ$ ] and  $\sim 43$ – $45 \pm 1^\circ$  [ $(\theta_a - \theta_r) \sim 4 \pm 1^\circ$ ] for alkanethiolate/Au{111}<sup>10</sup> and  $\sim 112$ – $114^\circ$  and  $\sim 45^\circ$  for octadecylsiloxane/SiO<sub>2</sub> SAMs.<sup>5–7</sup>

The contact angles for our

GaAs SAMs slowly decrease below  $n = 14$ – $15$ , eventually reaching values associated with poorly formed SAMs at  $n = 12$ . The dip in the hysteresis values for water (Figure 1B) for  $n = 16, 17$  suggests that there is a corresponding slight diminishing in the surface region organization for these SAMs; the HD hysteresis data, however, do not show this effect. Overall, the wetting data show that the surfaces of the longer chain SAMs are well organized with dense packing of the CH<sub>3</sub> groups. Finally we note that the water contact angle values depend on the measurement time. For example, within 10 min the contact angles on a C<sub>18</sub> SAM dropped from an initial value of  $112 \pm 2^\circ$  to  $94 \pm 6^\circ$ . This effect can be understood in terms of the ability of penetrated water molecules to etch the GaAs substrate and undercut the monolayer.<sup>55,56</sup>

### Permeability to O<sub>2</sub> from XPS Measurements of GaAs Surface

**Oxidation.** The Ga 3d and As 3d region spectra of the SAMs show main peaks centered at binding energies (BE) of 19.2 and 41.1 eV, respectively, which can be fit with two doublets assigned as the contributions from bulk Ga (19.0 eV) or As (40.9 eV) species and surface Ga (20.0 eV) or As (41.6 eV) species<sup>12,57</sup> (spectra shown in Supporting Information). No BE shift or peak broadening was observed as a function of chain length. To follow the oxidative stability, the freshly made SAMs were

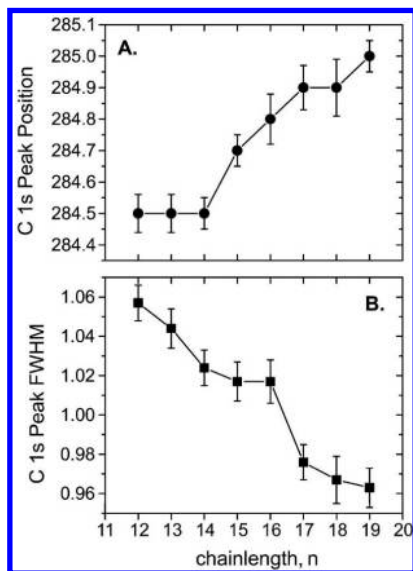


Figure 2. (A) XPS C 1s peak positions (eV). (B) FWHM (eV) for different length  $n$ -alkanethiols assembled on GaAs(001).

transferred to the XPS vacuum chamber within 5 min of preparation and immediately exposed to vacuum.

For  $n > 16$ , no oxidized surface species ( $\text{As}_x\text{O}_y$  or  $\text{Ga}_x\text{O}_y$ ) are observed, but for  $n < 16$ , an onset of a monotonic increase in oxidized species (more noticeably of  $\text{As}_x\text{O}_y$ ) with decreasing chain length is observed (see Figure 1C). Previous work<sup>12</sup> has shown that the  $\text{C}_{18}$  SAM is stable toward appearance of the oxidized species for at least 2 weeks of air exposure. For  $\text{C}_{16}$  and  $\text{C}_{12}$  monolayers,  $\sim 1\%$  and  $\sim 2\%$  of the total As 3d signal is from  $\text{As}_x\text{O}_y$  species, respectively, whereas 5% and 14% of the total As 3d signal is due to  $\text{As}_x\text{O}_y$  species, respectively, for freshly etched GaAs and native oxide surfaces.<sup>58</sup> Thus although alkanethiols are capable of removing residual oxidized species on freshly etched surfaces,<sup>12,44</sup> for  $\text{C}_{12}$  the amount of surface oxide forming immediately after monolayer formation is almost the same as that which forms on the freshly etched GaAs surface. These data indicate that  $\text{O}_2$  molecules penetrate into the SAM at increasing rates with decreasing chain length, consistent with the wetting data (Figure 1A), which point to increasingly poor organization of the alkyl chains with decreasing  $n$ .

**Adsorbate Coverage from XPS C 1s Spectra.** Analysis of the C 1s region of the monolayers shows that the C 1s BE peak decreases from 285.0 to 284.5 eV across the range of  $n = 19$ –12 while the associated peak full width at half maximum (FWHM) increases (Figure 2), similar to reported correlations for alkanethiolate SAMs on Ag and Au.<sup>59–61</sup> These trends have been attributed to electrostatic screening effects and do not reflect shifts in the chemical state of the C atoms.<sup>62</sup>

The main feature of interest is the correlation of the C 1s peak intensities (as integrated areas) with the  $n$  values. Because the C 1s cross section is constant for all the C atoms in the SAMs, for our condition of a  $90^\circ$  photoelectron exit angle (perpendicular to the substrate)

one expects a simple correlation based on the attenuation relationship:

$$I = \int_0^{z_d} \rho_o e^{-(z/\lambda)} dz \quad (1)$$

where  $z$  = distance into the alkyl chain matrix from the S–C interface towards the vacuum interface,  $z_d$  = the total thickness of the alkyl chain matrix,  $\rho_o$  = intrinsic C 1s photoelectron emission intensity per unit thickness  $(dI/dz)_o$  with no overlayer attenuation, and  $\lambda$  = C 1s photoelectron attenuation length for the alkyl chain matrix. Expressed in terms of a ratio to the  $\text{C}_{18}$  C 1s SAM intensity with  $\lambda = 35.4 \text{ \AA}$  and an alkyl chain matrix thickness increment of  $1.21 \text{ \AA}$  per C atom (per  $n$ ) gives  $I_n/I_{18} = 2.18 (e^{-0.0342n} - 1)$ .<sup>63</sup> As shown in Figure 1D, however, for  $n < 16$  the integrated C 1s intensity deviates to lower values. For example,

$$\frac{(I_{12}/I_{18})_{\text{exp}}}{(I_{12}/I_{18})_{\text{theory}}} = \frac{20.0}{[(31.1)(0.733)]} = 0.88 \quad (2)$$

where  $I_{18}$ ,  $I_{12}$  are the integrated C 1s peak intensities (see Figure 1D). This decrease can be attributed to a decrease of  $\sim 12\%$  in the C atom surface density (coverage) for the  $\text{C}_{12}$  compared to the  $\text{C}_{18}$  SAM. On this basis the correlation in Figure 1D shows a constant coverage for  $n \geq 16$  with deviations to lower surface coverage of  $\sim 4$ – $5\%$  for  $n = 15, 14$  and reaching  $\sim 8\%$  and  $12\%$  for  $n = 13$  and  $12$ , respectively.<sup>64</sup>

Attempts were also made to compute the C:S stoichiometries and sulfur coverage from the C 1s and S 2p signals.<sup>65</sup> However, because of the overlap of the S 2p region by the Ga 3s core level and As plasmons,<sup>12</sup> quantitative peak fitting of the S 2p region was problematic and no reproducible trends could be derived.

**Chain Conformational Ordering from IRS C–H Stretching Mode Frequencies.** Changes in the C–H stretching mode peaks with  $n$  provide a qualitative measure of the chain conformational order of each SAM and have been analyzed previously for the  $\text{C}_{18}$  SAM on GaAs(001).<sup>12</sup> For the longest chain length ( $n = 19$ ) these modes appear at  $2850 \text{ cm}^{-1}$  [ $-\text{CH}_2-$  sym str ( $d^+$ )],  $2878 \text{ cm}^{-1}$  [ $\text{CH}_3$  sym str ( $r^+$ ) split by Fermi Resonance (FR) interaction with the  $\text{CH}_3$  asym def],  $2917 \text{ cm}^{-1}$  [ $-\text{CH}_2-$  antisym str ( $d^-$ )], and  $2967 \text{ cm}^{-1}$  [ $\text{CH}_3$  asym in-plane str ( $r_a^-$ )] (see Figure 3). As observed in Figure 3, at low values of  $n$  both the  $d^-$  and  $d^+$  mode peaks show a shift to higher frequencies, a decrease in intensity and increased broadening, indicative of a decrease in the chain conformational ordering.

The peak frequencies are summarized in Table 1 and are compared to the data for the crystalline state of the  $\text{C}_{18}$  thiol dispersed in a KBr pellet and the liquid state of neat 1-dodecanethiol ( $\text{C}_{12}$ ). In general the agreement between the SAM and crystalline state  $d^-$  mode peak frequency values indicates that all of the



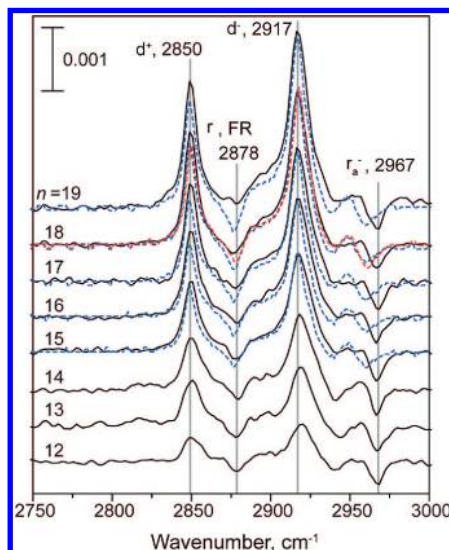


Figure 3. IRS spectrum as a function of chain length for *n*-alkanethiol monolayers on GaAs. The number of carbons atoms in the chain, *n*, is indicated. Vertical lines are drawn as a guide to the eye to show the shift in peak position ( $\text{cm}^{-1}$ ) for decreasing chain length with respect to the longest ( $n = 19$ ) chain. Simulated IRS spectra using a 2 chain per unit cell model with chains in an all-*trans* configuration (blue dotted lines) are included for comparison for chains  $n = 15$ – $19$ . An additional simulated spectrum showing the effect of incorporating 50% *gauche* defects into the terminal  $-(\text{CH}_2\text{CH}_3)$  group for the 2 chain per unit cell model is shown for  $\text{C}_{18}$  (red dotted line).

SAMs have significant degrees of conformational ordering, similar to the cases of alkanethiol molecules assembled on gold, silver, and copper surfaces.<sup>10,13</sup> The plot of the  $\text{d}^-$  peak position *versus*  $n$  in Figure 1E shows in more detail that for  $n \geq 16$  the peak frequencies level off in the  $2916$ – $2917 \text{ cm}^{-1}$  region, consistent with near limiting degrees of chain organization and conformational ordering,<sup>10,13</sup> whereas for  $n < 16$  there is a gradual increase in frequency with decreasing  $n$ , an indication of decreasing conformational order and monolayer organization with decreasing chain length. In turn, this overall structural trend with decreasing chain length is quite consistent with the decrease in surface organization (wetting data, Figure 1A), the increase in the permeation of  $\text{O}_2$  (XPS As 3d data, Figure 1C) and the decrease in adsorbate surface coverage (XPS C 1s data, Figure 1D).

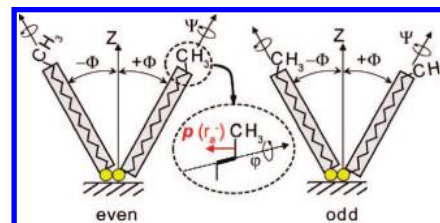


Figure 4. Schematics of laboratory and molecular coordinate frames for all-*trans*  $n\text{-C}_n\text{H}_{2n+1}\text{S}^-$  adsorbates on a surface, where  $n$  is even (left) and odd (right). The chain tilts are defined by angle  $\Phi$  from the surface normal, with the + and – directions indicated, and the twists (counterclockwise) around the long-chain axis by  $\Psi$ , with  $\Psi = 0$  for the C–C–C plane perpendicular to the surface plane, as shown. The inset in the center shows the terminal portion of the chain in the molecular coordinate frame. The rotation of the  $\text{CH}_3$  moiety around the adjacent C–C bond (bold line) to form *gauche* conformers is described by angle  $\phi$  with  $\phi = 0$  for the all-*trans* chain. The inset also shows the direction of the  $r_a^-$  mode transition dipole moment (red arrow), which lies in the C–C–C plane for the *trans* conformation.

#### Chain Orientations from IRS C–H Stretching Mode Intensities.

For all chain lengths, the  $\text{d}^-$  and  $\text{d}^+$  modes have positive absorbance features that increase in intensity, as expected, with increasing  $n$  (Figure 5). It has been previously established for the  $\text{C}_{18}$  SAM through analysis of the IRS  $\text{d}^-$  mode intensities and the NEXAFS spectra that the chains are extended in dominant all-*trans* conformations with an average  $14$ – $15^\circ$  chain tilt ( $\Phi$ ) and  $43^\circ$  twist ( $\Psi$ ).<sup>12</sup> For reference, coordinate frames are shown in Figure 4.

Application of the same IRS simulation analysis procedure to the  $\text{d}$  mode peaks in the present data set results in best fits for  $\Phi, \Psi = 15^\circ, 43^\circ$  for  $n > 15$ .<sup>66</sup> For  $n < 15$ , however, the quality of the best fits rapidly decays with decreasing  $n$  for model structures with possible tilt angles from  $0$ – $30^\circ$  and a range of twist angles.<sup>67</sup> The upper bound of  $\Phi = 30^\circ$  was used because our spectra simulations show that  $\Phi > 30^\circ$  results in inversion to negative absorbance features for both  $\text{d}$  modes.<sup>12</sup> The main discrepancy in the  $n < 15$  fits is due to the deviations in the peak positions and FWHM values (see Supporting Information), which is expected on the basis of the increasing conformational disorder for the shorter chains (see above), whereas the simulations are based on the optical function spectra obtained from

TABLE 1. Peak Positions for *n*-Alkanethiol C–H Stretching Modes in Crystalline and Liquid States and Adsorbed on GaAs(001)

	mode	bulk, $\text{cm}^{-1}$		$\text{C}_n\text{H}_{2n+1}\text{SH}$ on GaAs(001), $^\circ\text{cm}^{-1}$							
		crystalline <sup>b</sup>	liquid <sup>c</sup>	$n = 19$	$n = 18$	$n = 17$	$n = 16$	$n = 15$	$n = 14$	$n = 13$	$n = 12$
$\text{CH}_2$	$\text{d}^-$	2919	2925	2917	2917	2917	2918	2918	2918	2919	2920
	$\text{d}^+$	2849	2856	2850	2850	2850	2850	2850	2850	2851	2850
$\text{CH}_3$	$r_a^-$	2960 <sup>d</sup>	2961 <sup>d</sup>	2967	2967	2967	2967	2967	2967	2967	2967
	$r_b^-$	2949	2955	<i>e</i>	<i>e</i>	<i>e</i>	<i>e</i>	<i>e</i>	<i>e</i>	<i>e</i>	<i>e</i>
	$r^+$	2882 <sup>f</sup>	2872 <sup>f</sup>	2878	2877	2877	2879	2878	2879	2879	2879
	$r^+, \text{FR}$	2882 <sup>f</sup>	2872 <sup>f</sup>	2878	2877	2877	2879	2878	2879	2879	2879

<sup>a</sup>Peak positions were determined as an average for all independent spectra taken. Standard deviations for each reported peak position were  $\sim 0.2$ – $0.5 \text{ cm}^{-1}$ . <sup>b</sup>Crystalline-state positions were determined from the transmission spectra of  $\text{CH}_3(\text{CH}_2)_{17}\text{SH}$  dispersed in KBr. <sup>c</sup>Liquid-state positions were determined from the transmission spectra of  $\text{CH}_3(\text{CH}_2)_{11}\text{SH}$ . <sup>d</sup>The  $r_a^-$  mode is masked by the strong  $r_b^-$  feature in the crystalline- and liquid-state spectra but can be resolved by curve fitting. <sup>e</sup>The  $r_b^-$  mode is very weak as a result of orientation effects<sup>12</sup> and could not be observed because of signal to noise limitations. <sup>f</sup>The  $r^+$ , FR mode shows up as a shoulder on the  $\text{d}^+$  mode in the liquid-state spectra and is completely masked in the crystalline-state spectra but can be resolved by curve fitting.

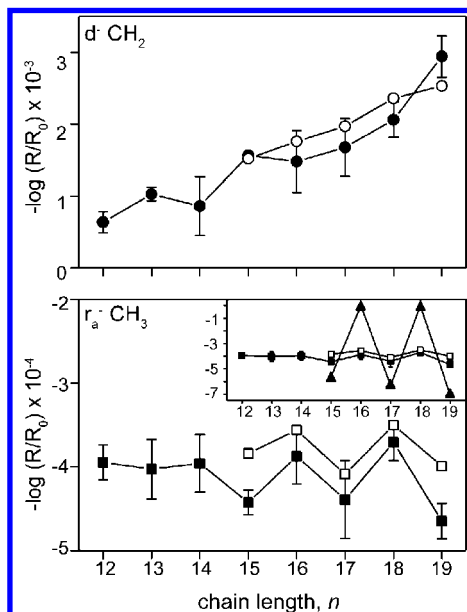


**Figure 5.** (Top) Intensity variance of the  $d^-$  mode with chain length. (Bottom) Intensity variance of the  $r_a^-$  mode. For both plots, open symbols represent simulated intensities obtained from a 2 chain per unit cell, all-*trans* model. Bottom Inset: Comparison of the simulated  $r_a^-$  mode intensities using a single chain per unit cell model (black triangles) with the experimental (black squares) and simulated 2 chain per unit cell model (black, open squares).

bulk polycrystalline state samples (pure thiol or disulfide).

While analysis of the  $d$  modes provides information on the structure of the main backbone, analysis of the  $r_a^-$  mode can provide information on the structure and orientation of the end  $\text{CH}_3$  group. There are two features to note. First, the  $d$  mode absorbance features remain positive for all  $n$ , whereas the  $r_a^-$  absorbance features remain negative (Figure 5). As reported previously,<sup>12,68</sup> this behavior can be understood on the basis of electromagnetic effects arising from the differences in the real parts of the complex refractive index tensor elements for the two types of modes. Second, for  $16 < n < 19$  the  $d^-$  absorbance intensities decrease nearly monotonically, whereas the  $r_a^-$  intensities show a distinct odd-even variation that disappears for  $n < 16$ . This variation can be straightforwardly interpreted in terms of the variation of the orientation of the  $-\text{CH}_3$  group with shifting from even to odd chain lengths while the  $-(\text{CH}_2)-$  backbone maintains a constant orientation (see Figure 4).

For the simulation of the  $r_a^-$  mode spectra the transition dipole moment direction is first fixed in the molecular coordinates with  $\varphi = 0$  (all-*trans* chain). For initial laboratory frame conditions of  $\Phi = 0$ ,  $\Psi = 0$  (chain axis parallel to  $z$  and no twist) the terminal  $\text{C}-\text{CH}_3$  bond is oriented  $+35.5^\circ$  from the  $z$ -axis. The simulations were carried out with two types of models: (1) a single chain representing the average structure of the molecules in the monolayer and (2) a pair of independently oriented chains representing the average structure for a mono-

layer with a 2-chain per unit cell structure. In the 2-chain model the final spectra were calculated as  $1/2(S_1 + S_2)$ , where  $S_1$  and  $S_2$  are the two individual spectra. For the simulations the chain tilts and twists were set to  $\Phi = +15^\circ$  or  $-15^\circ$  and  $\Psi = 43^\circ$ , respectively, to match the best fit chain orientation from the  $d$  modes, and the terminal  $-\text{CH}_3$  group then rotated at selected values of the angle  $\varphi$  around the adjacent  $\text{C}-\text{C}$  chain bond to break the planar character of the chain. Simulations were only carried out for  $n \geq 15$  where accurate fits of the chain tilt could be obtained (see above). A schematic of the coordinate frame and chain models is shown in Figure 4.

For the single chain model with  $\varphi = 0$  (all-*trans* chain), the simulations match the modulation character of the odd-even  $r_a^-$  intensity pattern only when the odd and even chains have tilts of opposite sign, viz.,  $\Phi_{\text{even}} = -15^\circ$  and  $\Phi_{\text{odd}} = +15^\circ$ . The magnitude of the intensity value modulation, however, is much too extreme to fit the experimental spectra; see Figure 5. Variation of the  $\text{CH}_3$  twist angle  $\varphi$  does not result in any significant improvement.

In contrast, an ideal all-*trans* ( $\varphi = 0$ ) 2 chain model with  $\Phi_{\text{even}} = -15^\circ$ ,  $\Psi_{\text{even}} = 43^\circ$  and  $133^\circ$  (a schematic of this model is shown in Figure 4) gives the best fits and is included for comparison with experimental spectra in Figure 3.<sup>69</sup> This structure is essentially a herringbone packing with a  $90^\circ$  setting angle between the  $\text{C}-\text{C}-\text{C}$  planes, similar to the well-known structure for alkanethiolate SAMs on Au{111} SAMs, which exhibit 2 chains per unit subcell (see Supporting Information for details).<sup>10,70</sup>

For chain lengths with  $n < 15$  the odd-even modulation of the  $r_a^-$  intensities vanishes. This cannot be explained by assuming that the chains have an increased cant, since an even more pronounced odd-even trend should be observed even if the chain tilt increases. Rather, this is consistent with the conclusions from the evidence in the previous sections that the chains become increasingly conformationally disordered with decreasing chain length, thus leading to a smearing of the distributions around the average molecular orientation parameters. A similar argument has been applied to alkanethiol monolayers on Au where *gauche* conformers diminished the odd-even effect observed in the  $r_a^-$  mode intensities.<sup>10</sup>

**Translational Ordering from GIXRD.** *GIXRD of the  $\text{C}_{18}$  SAM.* Bragg reflection scans on six independently prepared  $\text{C}_{18}$  SAM samples revealed two types of first-order Bragg reflection patterns, labeled **I** and **II** for reference, which depended on the specific sample. Both patterns represent the same unit cell symmetry and lattice spacings. The overall results are summarized in Table 2.

In pattern **I**, observed for most of the samples, the Bragg peak intensity showed maxima at nominal  $60^\circ$  azimuthal separations, an indication of preferential orientation of the thiol domains along hexagonal symme-

TABLE 2. Summary of Bragg Reflection Data for C18 SAM on GaAs(001)

Bragg reflection position ( $\text{\AA}^{-1}$ )	FWHM $\Delta q_{xy}$ ( $\text{\AA}^{-1}$ )	domain size, ( $\text{\AA}$ )	azimuthal positions of Bragg reflections ( $\phi$ ; ref to $\phi = 0$ for the [110] direction), deg		azimuthal separation between specific Bragg reflections ( $\delta\phi$ )	
			I <sup>a</sup>	II	I	II <sup>b</sup>
1.49	0.08	74	$\phi_A = 64$	$\phi_A = -31$		$\delta\phi_{AE} = 32$
			$\phi_B = -51$	$\phi_B = 40$	$\delta\phi_{AB} = 65$	$\delta\phi_{EB} = 39$
				$\phi_B = 61$	$\delta\phi_{BC} = 52$	$\delta\phi_{DC} = 67$
				$\phi_D = 90$	$\delta\phi_{CA} = 63$	$\delta\phi_{DE} = 53$
1.51	0.09	66	$\phi_C = 1$	$\phi_E = 128$		$\delta\phi_{CF} = 29$
				$\phi_F = 1$		$\delta\phi_{FD} = 38$
						$\delta\phi_{CE} = 60$
						$\delta\phi_{FA} = 21$

<sup>a</sup>I and II refer to the two monolayer structures described in the text. Structure I and II have azimuthal peak separations of  $\phi \pm \sim 60^\circ$  and  $\phi \pm \sim 30^\circ$ , respectively. <sup>b</sup>The azimuthal separations for structure II with reflections separated by nearly  $\sim 30^\circ$  and  $\sim 60^\circ$  are both considered; see text for details.

try. With the azimuthal angle  $\phi$  set to zero for the [110] reference direction (see Figure 11),<sup>74</sup> two of the reflections were observed at  $+19^\circ$  off the [100] direction ( $\phi = 64^\circ$ ) and  $-6^\circ$  off the [010] direction ( $\phi = -51^\circ$ ), both corresponding to  $q_{xy} = 1.49 \text{ \AA}^{-1}$  (Figure 6A).<sup>71,72</sup> The observed radial FWHM ( $\Delta$ ) of  $0.08 \text{ \AA}^{-1}$  for the two peaks yields an average domain size of  $\sim 74 \text{ \AA}$ .<sup>73</sup> In comparison, domain sizes of  $\sim 250$ ,  $\sim 120$ , and  $\sim 60\text{--}75 \text{ \AA}$  have been reported for alkanethiolates on Au{111}<sup>74</sup> and Ag{111}<sup>26</sup> and alkaneselenolates on Au{111}.<sup>75</sup> The third peak was observed at  $1^\circ$  off the [110] direction ( $\phi = 1^\circ$ ) to give a different diffraction spacing of  $q_{xy} = 1.51 \text{ \AA}^{-1}$  (Figure 6B). The associated  $\Delta q_{xy} = 0.09 \text{ \AA}^{-1}$  corresponds to a domain size of  $\sim 66 \text{ \AA}$ . The existence of two slightly different  $q_{xy}$  values and the deviations from exact  $60^\circ$  azimuthal peak separations (see Table 2) indicate a distorted or pseudo hexagonal structure.

Azimuthal rotation of the sample around each Bragg reflection peak setting showed an azimuthal  $\Delta\phi$  smearing with a FWHM  $= \sim 28^\circ$ . This value represents the orientational inhomogeneity of monolayer domains across the surface. In the case of a perfect powder, no independent azimuthal peaks would be observed; instead, the azimuthal scan would show a constant intensity corresponding to an in-plane powder ring. We note that  $\Delta\phi \approx 28^\circ$  is large compared to other SAM systems, which typically have  $\Delta\phi \approx 1\text{--}10^\circ$ <sup>26,29,75,76</sup> and are hence considered single crystalline. This result shows that there is only a weak azimuthal alignment of the thiol domains on GaAs compared to other SAM systems, e.g., alkanethiolate domains on Au(111).

In pattern II, five monolayer reflections are observed at  $\phi_{II} = -31^\circ, +1^\circ, +40^\circ, +61^\circ, +90^\circ$ , and  $+128^\circ$ . Overall, these peaks differ by steps of  $\phi_{II} \pm \sim 30^\circ$  instead of  $\phi_I \pm \sim 60^\circ$  observed for pattern I. The same lattice spacings along the same symmetry directions (see Supporting Information), however, are observed, with the monolayers aligning at  $+1^\circ$  from the [110] GaAs(001) substrate direction. The different azimuthal depen-

dence of the Bragg reflections in the two monolayer structures could be due to the presence of two different SAM domain alignments differing by  $30^\circ$ .<sup>26</sup> Note that the  $\sim 60^\circ$  separated reflections of  $60^\circ, 53^\circ$ , and  $67^\circ$  are close to the  $63^\circ, 52^\circ$ , and  $65^\circ$  spacings in pattern I, an indication that there are no significant differences in the derived unit cells. Attempts to determine the thiol form factor and thus the molecular tilt angle from the from the rod scans as a function of  $q_z$  proved inconclusive as a result of the broad nature

of the diffraction peaks.

Analysis of the  $\phi_I \pm \sim 60^\circ$  azimuthal dependence yields two different nearest neighbor (NN) distances,  $5.02 \text{ \AA}$  along the  $\phi = 91^\circ$  ( $90^\circ + 1^\circ$ , slightly off the  $[1\bar{1}0]$ , i.e.  $[\bar{1}10]$ ) and the  $\phi = 39^\circ$  ( $90^\circ + 51^\circ$ ) directions and  $4.70 \text{ \AA}$  along the  $\phi = 154^\circ$  ( $90^\circ + 64^\circ$ ) direction. These NN distances and their azimuthal separations ( $\delta\phi$ , see Table 2) lead to a reciprocal areal density of  $\sim 21.2 \text{ \AA}^2/\text{molecule}$ , slightly higher than the reciprocal areal density reported for SAMS alkanethiolates on Au ( $\sim 21.8 \text{ \AA}^2/\text{molecule}$ )<sup>10,25,28,77</sup> but less than the most dense phases observed for Langmuir films of fatty acids on water ( $\sim 17\text{--}19 \text{ \AA}^2/\text{molecule}$ ),<sup>78</sup> alkanethiolates on Hg

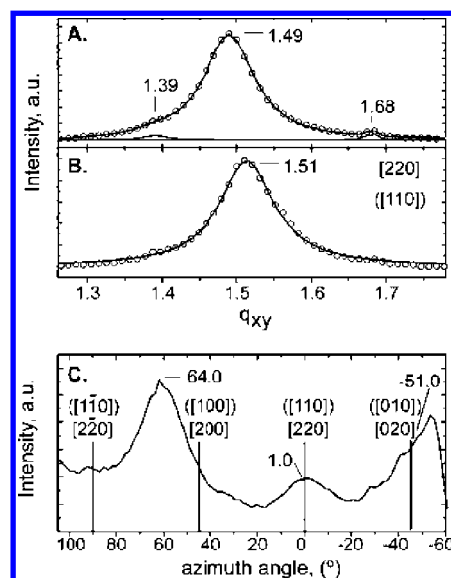


Figure 6. X-ray diffraction through the first-order diffraction peaks of the C<sub>18</sub> monolayers GaAs(001) as a function of  $q_{xy}$ . (A) A monolayer reflection with  $q_{xy} = 1.49 \text{ \AA}^{-1}$ . (B) Along the [110] direction, the monolayer reflection is observed at  $q_{xy} = 1.51 \text{ \AA}^{-1}$ . (C) The azimuthal orientation ( $\phi$ ) of the C<sub>18</sub> monolayer reflections with  $\Delta\phi \approx 60^\circ$ . The position of the substrate directions are marked with a vertical line. The monolayer reflections are observed  $1^\circ$  off the [110] direction ( $\phi = 0^\circ$ ) with subsequent peaks oriented  $\phi = 64^\circ$  and  $-51^\circ$ , corresponding to  $\delta\phi = 63^\circ$  and  $52^\circ$ , respectively. See text for details.

( $18 \text{ \AA}^2/\text{molecule}$ ),<sup>79</sup> or even octadecyltrichlorosilane (OTS) monolayers on  $\text{SiO}_2$  surfaces ( $\sim 20 \text{ \AA}^2/\text{molecule}$ ).<sup>80</sup> Figure 7A depicts the proposed lattice structure superimposed on an ideal unreconstructed, As terminated GaAs(001) surface with the  $[1\bar{1}0]$  direction indicated for reference. The schematic incorporates the 2-chain per unit cell herringbone structure as predicted by the IRS spectra. A representation of the pseudo-hexagonal unit sub cell is shown in Figure 7B. Note that none of the NN distances of the SAM monolayer structure correspond within errors to the NN distance ( $3.995 \text{ \AA}$ ) or the next nearest neighbor (NNN) distance ( $5.65 \text{ \AA}$ ) of the intrinsic GaAs(001) square lattice plane and thus the monolayer is highly incommensurate with the intrinsic substrate surface lattice. Given the preferential alignment of the adsorbate molecules along the  $[1\bar{1}0]$  direction and the previously established direct bonding to the substrate, primarily at As sites,<sup>12,44,46,51,53,54</sup> it appears that the process of monolayer formation involves a combination of chemical bonding and restructuring of the intrinsic GaAs(001) surface, driven by the intermolecular packing forces. The steps necessary to achieve full covalent bonding are suggested in Figure 7C. Preferential alignment of adsorbates along the  $[1\bar{1}0]$  step edge direction of GaAs(001) has been observed for many systems including  $\text{C}_{60}$ <sup>81,82</sup> and various chalcogenides.<sup>83,84</sup> The scanning tunneling microscopy observation that the step edges on the (001) surface run parallel to this direction<sup>81</sup> imply that the high energy step edge atoms are the preferred initial binding sites of adsorbate molecules.

**GIXRD of the  $\text{C}_{12}$  SAM.** Because the contact angle and XPS and IRS data of the  $\text{C}_{12}$  monolayers indicated a reduced degree of organization and coverage relative to the SAMs with  $n > 15$ , GIXRD measurements were made on  $\text{C}_{12}$  SAMs to compare the translational order to the  $\text{C}_{18}$  case. Analysis of a number of samples at different spots for the  $\text{C}_{12}$  SAMs showed no evidence of Bragg reflection from the monolayer (see Supporting Information). Even along the high-symmetry  $[1\bar{1}0]$  direction where the  $\text{C}_{18}$  SAMs were observed to align, no monolayer reflections were observed. Since the presence of the monolayer was confirmed by SWE and IRS measurements, the absence of any reflections indicates that no significant translational order exists.<sup>85</sup> For completeness, a wide azimuthal scan was taken and only out of plane reflections along the  $[1\bar{1}0]$  directions arising from the GaAs (111) scattering rod are observed; no monolayer peaks were observed (see Supporting Information).

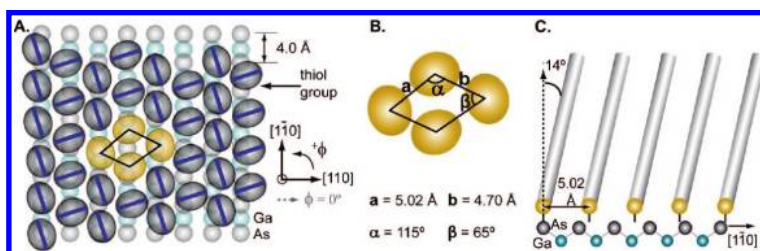


Figure 7. (A) The molecular unit cell embedded in a larger, *ideal* monolayer overlayer structure. The monolayer structure is shown in real space with respect to an ideal intrinsic As-terminated (001) GaAs surface. The gray ellipses represent top down vertical projections of untilted thiolate chains onto the substrate plane with the C–C–C planes indicated as blue bars. The relative twists of the chains show the herringbone pattern deduced from the IRS data. (B) Representation of a unit subcell and the associated lattice parameters. (C) Schematic side view representation of the monolayer structure along the  $[1\bar{1}0]$  substrate direction. Note that the  $5.02 \text{ \AA}$  adsorbate spacings determined from GIXRD do not match the ideal As atom spacings along the  $[1\bar{1}0]$  direction in the intrinsic (001) substrate plane. Given the presence of S–As chemical bonds, this mismatch implies the As atoms must shift and reorganize during chemisorption of the alkanethiols to accommodate the molecular spacing.

**Comparison of a  $\text{CH}_3$ -Terminated Aromatic Thiolate Monolayer to Alkanethiolate Monolayers on GaAs(001).** *Adsorbate Molecule Orientation by IRS.* The IRS spectra of MBT molecules self-assembled on GaAs(001), and on Au{111} for comparison, are shown in Figure 8. The highly metallic Au substrate results in positive absorbance features; in contrast the GaAs substrate shows both positive and negative features.<sup>12,68</sup> These differences are expected on the basis of the specific optical conditions and the different complex dielectric functions of these two materials.<sup>68,86</sup> To assist in assigning the vibrational modes and determining the orientation of their respective transition dipole moments, a normal mode analysis was done using DFT calculations for a single, isolated MBT molecule with an optimized geometry. Because the resulting geometry predicts a  $37^\circ$  twist of ring 2 (connected to the methyl group; see Figure 9) with respect to ring 1 (connected to the thiol), this geometry was utilized for assigning the modes and transition dipole directions. The mode assignments, frequencies and transition dipole moment directions of the major peaks are summarized in Table 3. The transition dipole moments were assigned by direct inspection of the nor-

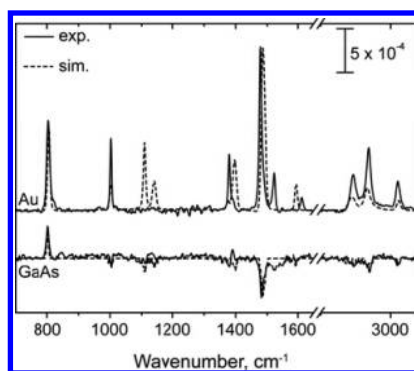
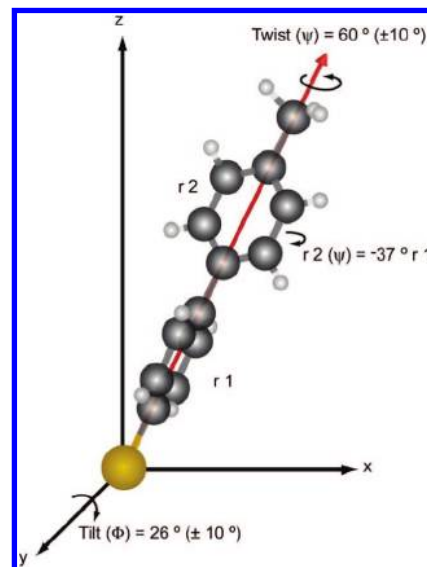


Figure 8. IR spectrum of MBT on Au and on GaAs. The IR spectrum of the monolayer assembled on Au is included for comparison. Identification of these peaks is presented in Table 3.



mal mode motions. The effect of variation of the twist of ring 2 shows up primarily in the r1, r2 aryl C–H in plane stretch modes.

Using the standard simulation procedure<sup>68</sup> based on the assigned transition dipole moment directions and the optical function spectra obtained from analysis of spectra of polycrystalline MBT dispersed in KBr pellets, the orientations of the MBT molecules on the GaAs(001) and Au surfaces were derived. The SAM monolayer thickness on both surfaces was initially set to 12.4 Å (derived from the untilted DFT optimized geometry molecular length of 10.5 Å, corrected for the 1.94 Å S-atom thickness contribution<sup>87</sup> and the resultant value subsequently adjusted for each new simulated molecular tilt angle).<sup>88</sup> Analysis of the modes with transition dipoles oriented parallel to the main longitudinal axis of the MBT molecule yielded a tilt ( $\Phi$ ) of  $26^\circ \pm 10^\circ$  for this axis from the surface normal for both SAMs, showing good consistency with NEXAFS derived values of  $\Phi = 30^\circ$  for MBT SAMs on GaAs(001) surfaces,<sup>54</sup> though slightly larger, but within error, of the  $\Phi = 19^\circ$  derived tilt angle from grazing incidence X-ray diffraction (GIXRD) experiments for MBT SAMs on Au surfaces.<sup>50</sup> Analysis of the modes with transition dipoles oriented perpendicular to the long axis and in and out of the plane of the ring 1 gave best fit values of  $\Psi = 55^\circ \pm 10^\circ$  on Au surfaces and  $\Psi = 60^\circ \pm 10^\circ$  on GaAs(001) surfaces for the twist angle of ring 1 with ring 2 fixed at  $37^\circ$  from ring 1. Attempts to fit the spectra with parallel rings gave comparatively poor fits in which the r1, r2 aryl C–H in plane modes show significantly increased deviations from the experimental values. Therefore, we conclude that the optimized geometry derived from DFT calculations represents the conformation of the MBT molecules in the SAM structure.



**Figure 9.** Representation of the 4'-methyl-biphenyl-4-thiol (**2**) molecule oriented in a coordinate system in which the  $x$ - $y$  plane represents the substrate surface. The molecule is initially oriented with ring 1 (r1, attached to the thiol) in the  $x$ - $z$  plane and ring 2 (r2, attached to the methyl) is twisted  $-37^\circ$  into the  $x$ - $y$  plane from ring 1. The final configuration, as shown in this figure, is defined by a twist ( $\Psi$ ) of the entire molecule about the  $z$ -axis and a tilt ( $\Phi$ ) about the  $y$ -axis in the  $x$ - $z$  plane. The best fit value of the angles determined from IR measurements of this molecule assembled on a GaAs(001) surface are indicated.

Although the  $26^\circ$  molecular tilt angle of the MBT SAMs on GaAs(001) is markedly different from the low values for the alkyl SAMs with  $n > 15$ , it agrees well with the  $30^\circ$  molecular tilt angle from NEXAFS measurements<sup>54</sup> and is close to the tilt angles reported for SAMs of similar molecules, terphenyldithiol and quaterphenyldithiol, on GaAs.<sup>89</sup> The  $26^\circ$  molecular tilt angle of the MBT SAMs on Au is slightly larger than the  $19^\circ$  tilt angle

measured for MBT SAMs from grazing incidence X-ray diffraction (GIXRD) experiments<sup>50</sup> but is, within error, similar to the tilt angle derived for other biphenyl thiolate SAMs homologues measured by NEXAFS.<sup>49</sup> The implications of the different molecular tilts with regards to SAM structure on each surface are deferred to the Discussion section.

There is a general agreement in the peaks observed in the experimental IRS spectra for the MBT SAMs assembled on GaAs(001) and Au surfaces with respect to their simulated IRS spectra (see Fig-

**TABLE 3. Peak Assignments of MBT Monolayers Assembled on GaAs(001)**

mode assignment <sup>a</sup>	frequency, $\text{cm}^{-1}$			transition dipole direction <sup>c</sup>	peak direction <sup>d</sup>
	GaAs	Au	isotropic <sup>b</sup>		
r1, r2 aryl C–H str, ip	3023	3026	3028	in $x$ - $z$ plane of each ring	–
$\nu_{\text{asym}}$ CH <sub>3</sub>	2924	2921	2917	$z$	–
$\nu_{\text{sym}}$ CH <sub>3</sub>	2864	2866	2857	$z$	–
r1 or r2 ( $\nu_{9a}$ )	1599	1612	1594	$z$	–
	1526	1521	n.o.	$z$	–
r1, r2 ( $\nu_{18a}$ )	1492, sh	1486, sh	1492	$z$	–
$\delta_{\text{asym}}$ CH <sub>3</sub>	1482	1478	1484	$z$	–
r1, r2 ( $\nu_{18b}$ ), $\delta_{\text{asym}}$ CH <sub>3</sub>	1390, sh	1393, sh	1394	$z$	derivative
$\delta_{\text{sym}}$ CH <sub>3</sub>	1381	1379	1376	$z$	derivative
r, r2 ( $\nu_{14a}$ )	1148	n.o.	1139	$z$	–
r1, ( $\nu_{19a}$ )	1108	n.o.	1109	$z$	–
r2-CH <sub>3</sub> ring deformation	1004	1002	1002	$z$	–
aryl C–H op, r1, r2 ( $\nu_{17b}$ )	803	805	805	$y$	+

<sup>a</sup>The mode assignments are made using the DFT calculations and are described according to what the literature commonly suggests for modes in these positions. r1 refers to the ring attached to the thiol, and r2 refers to the ring attached to the methyl.

<sup>b</sup>Bulk peak positions were determined from the simulating a 12 Å isotropic film of **2** on a Au surface. <sup>c</sup>Approximate dipole directions were determined from DFT calculations. See text for details. <sup>d</sup>The peak directions refer to the direction of the peaks in the GaAs spectra. All peaks were observed to be positive in the Au spectra. Abbreviations used: n.o. = not observed; sh = shoulder; str = stretch; ip = in the plane of the respective ring.

ure 8) and with respect to the isotropic spectra derived from the bulk optical constants (see Table 3). There are several inconsistencies, however. First, in both the GaAs and Au SAMs a new peak is observed at  $\sim 1522\text{ cm}^{-1}$  that is not observed in the bulk spectra. At this point, the exact identification of this mode is unknown, but it may be a very weak mode that we observe in the normal mode analysis from the DFT calculations but is enhanced when the molecule assembles and becomes constrained by other molecules on the surface. Second, neither the  $1108.5$  nor the  $1139.2\text{ cm}^{-1}$  mode is observed in the IRS spectra of the MBT SAMs on Au surfaces, although they are observed as weak features on GaAs(001) surfaces. This is particularly surprising since both modes have z-oriented transition dipole moments, which, given the same molecular orientation and the observation of all other z-oriented transition dipole moments on both GaAs(001) and Au, should also be observed on both surfaces.

Finally, we note that the derivative shapes in the observed at  $1380.6$  and  $1390.1\text{ cm}^{-1}$  peaks in the GaAs SAM spectra are not observed in the simulations. This likely indicates that the exact dipole directions lie slightly out of the z-direction and corrections would be needed in the simulations to account for this deviation from the assumed directions.

**Permeability to  $\text{O}_2$  from XPS Measurement of GaAs Surface Oxidation.** XPS spectra of the Ga 3d and As 3d regions reveal spectra with similar attenuation intensities observed from the  $\text{C}_{12}$  monolayers and similar oxidation of the GaAs substrate (see Supporting Information). Approximately 3% of the As 3d signal was determined to

be due to  $\text{As}_x\text{O}_y$ . This is approximately the same amount (2%) of substrate oxidation observed after assembly of the  $\text{C}_{12}$  alkanethiolate monolayers and also observed from previous HRXPS measurements of MBT SAMs on GaAs(001).<sup>53</sup> These data show that the MBT and  $\text{C}_{12}$  SAMs exhibit similar permeabilities to  $\text{O}_2$  and thus presumably have similar packing densities.

**Translational Ordering by GIXRD.** The single weak, broad diffraction peak in Figure 10 occurs at  $q_{xy} = 1.41\text{ \AA}^{-1}$  along the [100] direction of the GaAs(001) substrate and corresponds to a NN distance of  $5.10\text{ \AA}$ . The associated peak width  $\Delta q_{xy} = 0.23\text{ \AA}^{-1}$  corresponds to a small domain size of  $\sim 29\text{ \AA}$ . An additional peak, of unknown origin was observed at  $q_{xy} = 1.29\text{ \AA}^{-1}$  in this scan and extended across all values of  $q_z$ .<sup>71</sup>

Along the [110] direction of the GaAs(001) substrate, a larger lattice spacing of the monolayer was observed. In Figure 10 a weak, broad, in-plane reflection corresponding to the monolayers is observed at  $q_{xy} = 1.32\text{ \AA}^{-1}$ , corresponding to a lattice spacing of  $5.54\text{ \AA}$  along the  $[\bar{1}\bar{1}0]$  symmetry direction. From the fit of the integrated intensity of this peak (see Figure 10) a peak width  $\Delta q_{xy} = 0.19\text{ \AA}^{-1}$  was determined, corresponding to a small domain size of  $\sim 31\text{ \AA}$ . A Bragg reflection from the (11 $\bar{l}$ ) scattering rod of the GaAs(001) substrate at  $q_{xy} = 1.54\text{ \AA}^{-1}$  is also observed.

The lattice spacings observed for the MBT SAMs on GaAs(001) are significantly larger than those observed for  $\text{C}_{18}$  SAMs on GaAs(001). Along the [100] direction, a spacing of  $5.10\text{ \AA}$  was observed, close to the lattice spacing ( $4.97\text{--}5.20\text{ \AA}$ ) predicted for the  $\sim 25\text{--}30^\circ$  molecular tilt angle determined by NEXAFS<sup>53</sup> and IRS modeling measurements. Furthermore, the intensities are much weaker and the domain sizes much smaller than those observed for the  $\text{C}_{18}$  SAMs on GaAs(001). This indicates little order is present within the MBT monolayers, consistent with the susceptibility of the SAM to oxidation. The  $5.54\text{ \AA}$  lattice spacing observed along the [110] symmetry direction of GaAs is nearly the same dimension as the NNN distance of the GaAs(001) substrate ( $\sim 5.65\text{ \AA}$ ) and may be a result of the MBT monolayers binding to specific intrinsic substrate sites along this direction.

These data show that the structure of the MBT monolayers on GaAs(001) is much different than the structure of the same SAMs on Au.<sup>50</sup> On Au, two phases were reported: a dense, upright, hexagonal phase and a less dense striped phase.<sup>50</sup> In the upright, hexagonal phase, smaller tilt angles ( $\sim 19^\circ$ ) and lattice spacings ( $\sim 5\text{ \AA}$ ) were observed. These differences are counterintuitive based on the larger tilt angles and NN distances observed for alkanethiols on Au{111} surfaces versus the smaller tilt angles and NN distances observed for alkanethiols on GaAs. This indicates that intermolecular interactions are particularly important for determining the final monolayer structure of SAMs on GaAs.

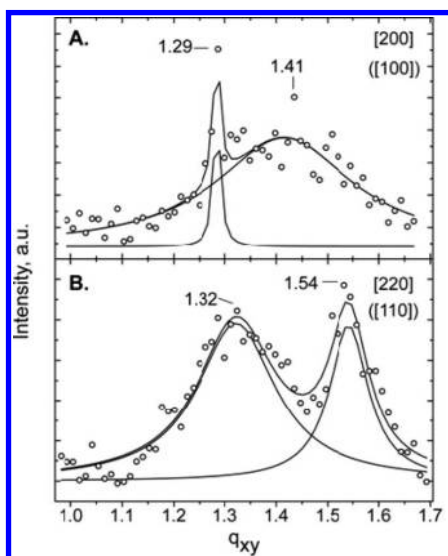


**Figure 10.** First-order diffraction peaks of the MBT monolayers along the [100] and [110] directions of GaAs(001) as a function of  $q_{xy}$ . (A) Along the [100] direction, a weak monolayer reflection is shown at  $q_{xy} = 1.41\text{ \AA}^{-1}$ . An additional peak, of unknown origin was also observed at  $q_{xy} = 1.29\text{ \AA}^{-1}$ .<sup>71</sup> (B) Along the [110] direction, a weak monolayer reflection is shown at  $q_{xy} = 1.32\text{ \AA}^{-1}$ . The (11 $\bar{l}$ ) scattering rod of the GaAs(001) substrate at  $q_{xy} = 1.54\text{ \AA}^{-1}$  is also observed in this scan.

## DISCUSSION

The discussion is organized as follows: First we discuss the results for the alkanethiolate monolayers, starting with those for the long chains with  $n > 15$  and moving to the short chains ( $n = 12-15$ ). Next we discuss the MBT monolayer results and finally make some general conclusions about the differences between the aliphatic and aromatic structures.

**Alkanethiolate SAMs. Long Alkyl Chain SAMs: Chain Packing Forces Drive Formation of Ordered, Incommensurate Structures.** For the homologous series of alkanethiolate monolayers assembled on GaAs(001), the combination of wetting, XPS, IRS, and GIXRD measurements are all consistent with a structural trend in which for chains longer than  $\sim 15$  carbons ( $n > 15$ ) the monolayers are highly organized with the chains conformationally ordered and arranged in a herringbone type of packing, similar to the structures of well-formed assemblies on Au{111}.<sup>10,90</sup> This type of packing is reminiscent of the simple unit subcell of a rhombohedral-like symmetry alkane crystal<sup>91,92</sup> in which each subcell has two chains with the C–C–C plane of one chain rotated  $\sim 90^\circ$  around the long axis relative to the orientation of the other chain plane (the setting angle). Our previous NEXAFS data<sup>12</sup> establishes that the chains are near vertically oriented with an average chain tilt angle of  $14-15^\circ$ , fully consistent with a quantitative analysis of the present IRS data. Finally, the GIXRD data for the **C<sub>18</sub>** SAM show the presence of distinct translational ordering of the adsorbate. Analysis of the Bragg reflection peaks observed at slightly off  $\sim 30^\circ$  and/or  $\sim 60^\circ$  intervals leads to a pseudo hexagonal unit cell exhibiting NN spacings of 4.70 and 5.02 Å (see Figure 7), domain sizes of  $\sim 66-74$  Å, and packing densities of  $21.2 \text{ Å}^2/\text{molecule}$ .

A striking aspect of this structure is the strong mismatch between the NN adsorbate spacings in the near hexagonal symmetry adsorbate lattice and the 3.995 and 5.65 Å NN and NNN spacings of As (or Ga) atoms in the intrinsic square symmetry (001) substrate surface plane. Given the previously established direct substrate atom–S chemical bonding,<sup>12,44,46,51,53,54</sup> primarily to As atoms, it is clear that the substrate surface atoms must shift positions during the assembly process in order to accommodate the placement of the As–SC<sub>18</sub>H<sub>37</sub> moiety in an ordered arrangement while maintaining a fixed As–S bond distance. The spacing mismatch is illustrated schematically in Figure 7C. The small domain correlation lengths ( $\sim 70$  Å) can be understood in terms of insufficiency of the chain packing forces to completely drive substrate surface lattice restructuring to a fully reconstructed structure commensurate with the lowest energy chain packing structure. Thus as the domains grow, the hexagonal molecular packing structure starts to decay as the substrate lattice spacings cannot fully accommodate. This would result in the tendency for a “tufted” chain structure to start forming to maintain chain packing at the grow-

ing domain edges and finally a break in domain growth as the tufted structure can no longer bridge to an adjacent molecular domain.

In considering this type of interplay between the chain packing forces and the compliance of the GaAs surface lattice it is useful to examine the limiting case given by the upright phase assemblies of alkyl chain molecules on liquids where the structurally featureless surface imparts high adsorbate mobility, provides no energetically favored pinning sites and leads to dominant chain packing driven assembly. Reported GIXRD experiments of Langmuir films of alkyl chain molecules adsorbed on liquid surfaces, including long fatty acids or alcohols on water,<sup>78</sup> fatty acids on liquid Hg,<sup>93–95</sup> and alkanethiolates on liquid Hg,<sup>79</sup> reveal common packing trends for these systems as the chains approach their most dense phase. For the upright phases in the lower density packing range, the molecules can be described generally as face centered rectangular or non-centered rectangular unit cells with tilted chains ( $\sim 25-30^\circ$ ). As the molecules are forced closer together under surface compression, they shift to well ordered hexagonal unit cells with the chains oriented nearly perpendicular ( $< 10^\circ$ ) to the substrate. For all these systems (at constant temperature) the phase transition to a hexagonal structure occurs when the molecules are packed  $\geq 20-21 \text{ Å}^2/\text{molecule}$ ,<sup>78,79,93–95</sup> similar to the  $21.2 \text{ Å}^2/\text{molecule}$  reciprocal areal density for the **C<sub>18</sub>** SAMs on GaAs(001).

In greater detail, Langmuir phases can be rich in substructure with observable differences in packing densities, tilt angles, correlation lengths, and translational order as compression increases to approach the final densest packed phase. These differences, described in detail in a comprehensive review,<sup>78</sup> reveal the delicate balance between inter-molecular chain interactions and substrate-head group interactions in the final monolayer structure. For example, for Langmuir films of long-chain fatty acids absorbed on water surfaces, order is induced by the interchain interactions ( $\sim 2-4 \text{ kT per CH}_2$ )<sup>96</sup> which dominate over the hydrogen bonding ( $\sim 15-21 \text{ kT}$ )<sup>97</sup> between the carboxylic head groups and the water interface. As a result, long translational correlation lengths ( $> 1000 \text{ Å}$ ) and NN spacings of  $\sim 4.84 \text{ Å}$  in the dense hexagonal phase are observed.<sup>78</sup> In contrast, Hg-supported alkanethiolate Langmuir films, which have a strong Hg–S liquid–head group interactions ( $\sim 200 \text{ kJ/mol}$ )<sup>98,99</sup> reminiscent of the As–S binding energy ( $\sim 400 \text{ kJ/mol}$ ) for the **C<sub>18</sub>** SAMs on GaAs(001),<sup>98,99</sup> have very short translational correlation lengths ( $< 90 \text{ Å}$ ) in the hexagonal phase but NN spacings ( $4.84 \text{ Å}$ ) similar to those of the carboxylic acid Langmuir films.<sup>79</sup> The short correlation lengths of the alkanethiolate–Hg films, similar in magnitude to those of the **C<sub>18</sub>** SAMs on GaAs(001) ( $\sim 66-74 \text{ Å}$ ), have been attributed to a frustrated packing of the alkyl chains imparted by the influence of

strong S-Hg-S bonds that form at the molecule–liquid interface.<sup>79</sup>

It is also useful to compare the GaAs(001) case to other structures of monolayers formed on surfaces that cannot provide an ordered template, such as octadecyl siloxane (ODS) on highly hydrated SiO<sub>2</sub>,<sup>80</sup> Langmuir–Blodgett (LB) fatty acid films on the hydrated native oxide surfaces of Cu and Ag and LB fatty acid films on Au.<sup>100</sup> Unlike the **C**<sub>18</sub> SAMs on GaAs(001), these monolayer systems show a simple, undistorted hexagonal structure but do show very small correlation lengths,  $\sim 45$  and  $\sim 140$  Å, respectively, similar to the **C**<sub>18</sub> SAMs on GaAs(001). The ODS monolayers are reported to exhibit a 4.84 Å NN spacing and a  $\sim 20.3$  Å<sup>2</sup>/molecule reciprocal areal density,<sup>80</sup> slightly smaller than the 4.9 Å and 20.8 Å<sup>2</sup>/molecule values observed for the fatty acids, regardless of the noble metal substrate.<sup>100,101</sup>

Although the close correspondence between the chain assembly structures on the limiting substrate-decoupled lattice pinning cases of liquid surfaces and the GaAs(001) substrate case could be taken to imply that the GaAs surface atoms are quite mobile (“liquid-like”), we also note the GIXRD data show a strong tendency for the SAM domains to align along the substrate  $[1\bar{1}0]$  crystal directions. This observation is consistent with a transitioning assembly mechanism in which the initial adsorbate thiols chemisorb at  $[1\bar{1}0]$  step edges in preference to the lower energy (001) surface plane and then subsequently seed domain growth across the (001) plane such that the emerging strong intermolecular packing forces dominate the overall SAM energetics and force substrate terrace atom restructuring.<sup>102</sup> This type of step edge nucleation mechanism has previously been proposed for LB films of fatty acids on single crystal noble metal surfaces where uniform alignment of the monolayers with the metal surfaces was observed during monolayer deposition.<sup>100</sup>

**Short Alkyl Chain SAMs: Chain Packing Forces Are Insufficient To Drive Formation of Ordered Structures.** For chain lengths  $n < 15$ , the conformational ordering, translational ordering, and packing of the alkane chains diminish, accompanied by a decrease in surface organization and resistance of the substrate to oxidation in air. These effects can be understood in terms of the reduced chain packing energies caused by the lower number of van der Waals interactions in the shorter chains. Following the film growth mechanism postulated above, it would follow that as the packing forces decrease with chain length, the ability of the intermolecular interactions to force restructuring of the GaAs substrate surface atoms would gradually decrease. The result would be decaying film order and decreasing coverages due to increasing NN spacings as the adsorbates shift gradually toward but never reach a limit of spacings and symmetry dictated by the intrinsic square (001) lattice. For the **C**<sub>12</sub> SAMs, it may be that they are close to the limit of a bonding to the intrinsic 5.655 Å NN sites. This is a large

lattice spacing at which significant disorder has been predicted in alkanes by molecular dynamics simulations<sup>103</sup> and is consistent with the absence of observable diffraction peaks. Thus, the final SAM structure appears to be a result of competition between specific binding sites on the intrinsic GaAs(001) surface and the drive to maximize the intermolecular interactions.

**MBT SAMs: Marginal Aromatic Ring Interactions Do Not Drive Dense Packing.** As with the case of long-chain alkanethiolate adsorbates, our GIXRD data show that the MBT SAMs on GaAs(001) adopt a hexagonal type of packing structure. In contrast though, the MBT SAMs exhibit lower coverages of 23–26 Å<sup>2</sup>/molecule and larger NN distances of 5.15–5.50 Å, while the IRS data indicate a larger 26° molecular tilt angle. Given the similar S–substrate bonding attachment in both cases, these differences can be interpreted in terms of the differences in minimum energy packing structures arising from alkyl chain *versus* phenyl ring  $\pi$ – $\pi$  interactions. Various biphenyl adsorbate molecules have been studied extensively on noble metal surfaces to elucidate the importance of intermolecular interactions, and it has generally been found that increasing the number of  $\pi$ – $\pi$  interactions drives the structures towards increasingly vertically oriented SAMs.<sup>49</sup> This suggests that the  $\pi$ – $\pi$  interactions in the MBT on GaAs(001) case are not sufficient to drive the structure to a near vertical orientation.

**Comparisons between Aliphatic and Aromatic SAMs and the Issues of Substrate Surface Atom Restructuring and Substrate Defects.** The effects of intermolecular interactions driving the structures of the thiolate SAMs on GaAs(001) can be seen clearly by looking at the limiting case of simple S-atom adsorption. Exposure of GaAs(001) surfaces to (NH<sub>4</sub>)<sub>2</sub>S<sub>x</sub> solutions results in simple (2 $\times$ 1)-S or (1 $\times$ 1)-S adlayers, commensurate with the underlying intrinsic GaAs(001) surface,<sup>39,40</sup> a stark contrast to the incommensurate alkanethiolate and MBT cases and definitive evidence that S-(GaAs) bonding itself does not drive any substrate surface reconstruction. An instructive comparison can be made with the cases of chemisorption of long-chain alkanethiolates and small S-containing species on Ag(111) surfaces wherein S, H<sub>2</sub>S, or CH<sub>3</sub>SH form a commensurate ( $\sqrt{7}\times\sqrt{7}$ ), R10.9° superlattice with a 4.4 Å NN spacing<sup>26,104</sup> while octadecanethiolate, with minimum intermolecular packing distances larger than the ( $\sqrt{7}\times\sqrt{7}$ ) NN spacings, forms an incommensurate, hexagonal adlayer with an expanded 4.7 Å NN distance.<sup>26,27</sup> Note that since the Ag(111) and Au(111) surfaces have near identical lattice spacings (2.89 Å), the alkanethiolate/Ag(111) overlayer might be expected to form a ( $\sqrt{3}\times\sqrt{3}$ ), R30° commensurate structure with  $\sim 30^\circ$  tilted chains, similar to the Au(111) case. Formation of an incommensurate overlayer occurs, however, to achieve a more closely spaced, less tilted phase.<sup>10</sup>

With this in mind, it is instructive to look more broadly at related cases in which chemically bonded overlayer structures form via a competition between in-



termolecular interaction driven substrate reconstruction and pinning at frozen sites on the intrinsic substrate lattice. At one extreme the final assembly structure approaches the limit of a free liquid substrate with no directed adsorbate bonding, whereas at the opposite extreme the assembly approaches the limit of a fully commensurate superlattice on the intrinsic substrate lattice. An example that shows the interplay of substrate bonding, substrate atom mobility and intermolecular interactions is given by MBT SAMs on GaAs(001), Au(111), and Hg surfaces.<sup>50,105</sup> On Au(111), the MBT molecules form a hexagonal unit cell with a reciprocal areal density of  $21.6 \text{ \AA}^2/\text{molecule}$  and NN distances of  $4.99 \text{ \AA}$ .<sup>50</sup> In contrast, the same molecules assembled on Hg have nearly the same reciprocal areal density as on Au surfaces ( $21.84 \text{ \AA}^2/\text{molecule}$ ) but instead form a rectangular unit cell structure with dimensions of  $5.56 \times 7.84 \text{ \AA}$ , very similar to the unit cell dimensions for the bulk biphenyl 3D structure.<sup>105</sup> We infer from this comparison that for Au(111) the substrate lattice remains essentially rigid with the thiolate moieties pinned at fixed lattice sites such that intermolecular interactions are only able to adjust secondary molecular packing, whereas for Hg the mobile substrate atoms allow the biphenyl intermolecular interactions to dominate the ordering. The structure of the MBT SAMs on GaAs(001) seems to be a hybrid of these cases for which both a hexagonal unit cell and NN distances on the order of the bulk MBT crystal are observed.

Substrate and adsorbate defects represent the inverse of the ordering character in a SAM and can be of critical importance in determining the performance of a SAM, *e.g.*, chemical and electronic passivation of a sensitive substrate. The effect of the chemisorbed monolayers on the chemical passivation (prevention of oxide growth) has been discussed earlier. Of particular interest here is the relevance to the longstanding interest in using surface treatments for precise control of the surface electronic properties (remove surface traps and unpin the Fermi level) of the GaAs(001) surface.<sup>106,107</sup> In our previous study<sup>44</sup> we showed that formation of a near limiting case of a highly organized **C<sub>18</sub>** thiolate SAM does not effectively passivate the electronic character of the GaAs(001) surface, which implies that critical surface defects are not removed by the assembly process. In light of the current results this observation can be understood in terms of a frustrated restructuring of the GaAs surface lattice, which results in short correlation lengths of the ordered **C<sub>18</sub>** SAM domains with extensive substrate surface atom defect domain boundary regions. This type of a mosaic structure provides a variety of possible surface trap sites that would defeat surface passivation. In accordance, we note that chemisorption of an inorganic S overlayer, which forms a simple commensurate structure with no indication of surface lattice restructuring, is considerably more effective in electrical passivation than an alkanethiolate SAM.<sup>44</sup>

Finally, we note that although we have been successful in forming SAMs with alkanethiols and MBT molecules on GaAs(001), attempts to form well-organized SAMs on GaAs with various other thiols, *e.g.*, aromatic thiols with electron-withdrawing substituents such as  $\text{NO}_2$ , have not been successful. We point out a possible explanation in terms of the variations of the strengths of the substrate atom–S(molecule) bonds caused by factors such as inductive and resonance effects. For example, one would expect that as the (molecule)S–As (or Ga) bond strength diminishes from substituent effects, it would become increasingly difficult for molecular packing forces to induce substrate restructuring, thus forcing the system towards the frozen pinning lattice limit with NN adsorbate spacings determined by the first arrangement available beyond the steric repulsion limit. In this case the secondary structure due to adjustment of molecular tilts and twists may not provide a sufficiently tight lattice to stabilize the adlayer against dissolution into solvent and/or oxidation of the underlying substrate, factors that would adversely affect coverages and organization.

## CONCLUSIONS

We have demonstrated that long-chain alkanethiols can chemisorb on GaAs(001) surfaces under simple solution conditions to form a mosaic structure of  $\leq 10 \text{ nm}$  domains oriented along the dominant step edge directions of the substrate surface and containing molecules packed in a fashion reminiscent of assemblies of alkyl chain molecules on liquid surfaces. The organization and coverage of these monolayers degrade as the chain lengths decrease below  $\sim 16$  total carbons. In comparison, the formation of a methyl biphenylthiolate SAM shows evidence of ordering with larger NN spacings and larger tilt angles than for the long-chain alkanethiolate SAMs. In all cases the final structures can be understood in terms of a balance between intermolecular packing forces, substrate–molecule bond strengths, molecular and substrate lattice matching, and substrate surface lattice forces. In the case of the long alkyl chains the strong molecule–substrate bonds and intermolecular interactions can force atoms in the intrinsic square symmetry GaAs(001) surface to adjust and restructure to form an incommensurate, pseudo hexagonal adsorbate lattice over short distances. In contrast, for the shorter chains the intermolecular forces are insufficient to drive significant substrate restructuring, which leads to a lower coverage, disordered structure. In the case of the MBT SAM the packing forces of the aromatic molecules are sufficient to form a weakly ordered structure but the NN spacings are greater than for the ordered long-chain alkanethiolate SAMs, an indication that the GaAs(001) surface atoms adjust to some extent to allow a stable MBT packing. Overall, this study reveals the subtle but

critically important balance between intermolecular, interfacial, and lattice forces that arises in molecular chemisorption on GaAs surfaces and suggests that

such effects need to be thoroughly considered in order to understand the properties of SAM systems on a variety of different types of substrates.

## EXPERIMENTAL METHODS

**Materials.** Ethanol (Pharmco, A.C.S./U.S.P. grade) was degassed through multiple freeze-pump-thaw cycles and stored in a closed container in a nitrogen gas purged glovebox between uses. Water was purified to remove organic and ion impurities (Milli-Q grade water; Millipore Products, Bedford, MA). Ammonium hydroxide (JT Baker, CMOS grade, 30%  $\text{NH}_4\text{OH}$  in water) and hexadecane (Sigma-Aldrich, 99+% anhydrous) were used as received.

Two types of GaAs(001)  $\pm 0.5^\circ$  substrates were used for monolayer formation: undoped double side polished and single side polished  $n^+$ -type doped wafers (Si dopant,  $0.8\text{--}4 \times 10^{18}/\text{cm}^3$ , prime epi-ready grade, American Xtal Technologies, Fremont, CA). Two-inch  $n^+$ -type GaAs wafers were used for reflection IR; undoped wafer samples ( $\sim 1 \times 1 \text{ cm}^2$ ) were used for all other studies; both types of wafers were used as received. No differences were observed between the SAM properties for doped and undoped wafers.

**Synthesis of Alkanethiols.** Alkanethiols  $\text{C}_n\text{H}_{2n+1}\text{SH}$  ( $n = 12, 15, 16$ , and  $18$ ) were obtained from Aldrich Chemical Co. (Milwaukee, WI) and were used as received. Potassium thioacetate, 1-bromotridecane, 1-bromotetradecane, 1-bromoheptadecane, and 1-bromononadecane, used to synthesize all other alkanethiols ( $n = 13, 14, 17$ , and  $19$ ) were obtained from Fluka Chemical Corp. (Milwaukee, WI). Nucleophilic substitution of alkyl bromides with potassium thioacetate yielded the corresponding alkane thioacetates.<sup>10,108</sup> The alkane thioacetates were hydrolyzed using 4 N NaOH to obtain the respective alkanethiols. The products were purified by column chromatography and were characterized by NMR and GC/MS.

**Synthesis of 4'-Methyl-biphenyl-4-thiol (2).** The title compound was obtained in two steps as described in Scheme 1. First, 4'-bromo-4-methyl-biphenyl **1** was synthesized by a Suzuki coupling reaction between 1-bromo-4-iodobenzene and 4-tolylboronic acid.<sup>109–114</sup> The bromo derivative was then converted to corresponding thiol **2** using  $n\text{-BuLi}$ , elemental sulfur, and concentrated HCl.<sup>115–118</sup>

**4'-Bromo-4-methyl-biphenyl (1).** In an oven-dried flask under dry nitrogen atmosphere was suspended  $\text{Pd}(\text{PPh}_3)_4$  (765 mg, 0.66 mmol, 3 mol%) in 100 mL of degassed toluene. 4-Tolylboronic acid (3.0 g, 22.06 mmol), 1-bromo-4-iodobenzene (6.24 g, 22.06 mmol), and sodium carbonate (2.34 g, 22.06 mmol) in degassed water were added to the above mixture in sequence. The brown solution was refluxed for 6 h and allowed to stir overnight at room temperature. The reaction flask was then cooled in an ice bath to obtain a grey/white precipitate. The mixture was decanted into a separatory funnel and extracted with hexanes. The organic phase was washed with  $2 \times 30 \text{ mL}$  of brine and  $2 \times 30 \text{ mL}$  of water. The solvent was dried over anhydrous sodium sulfate and purified by column chromatography using silica gel stationary phase and hexanes as the eluent to give 4.77 g of the bromide **1** in 88% yield.  $^1\text{H}$  NMR (300 MHz,  $\text{CD}_2\text{Cl}_2$ )  $\delta$  (ppm): 2.38 (s, 3H), 7.26 (d, 2H), 7.55 (d, 2H), 7.46 (d, 4H).  $^{13}\text{C}$  NMR (125 MHz,  $\text{CDCl}_3$ )  $\delta$  (ppm): 121.5, 126.9, 127.6, 128.66, 128.82, 131.82, 139.97, 140.12. GC/MS:  $m/z = 246$ .

**4'-Methyl-biphenyl-4-thiol (2, MBT).** In an oven-dried two-neck flask was dissolved 4'-bromo-4-methyl-biphenyl (**2**, 3.58 g, 14.49 mmol) in 35 mL of dry THF under positive nitrogen pressure, and the mixture was cooled to  $-78^\circ\text{C}$ . Then 2.5 M  $n\text{-BuLi}$  (5.8 mL, 14.49 mmol) was added dropwise over 20 min. The mixture was stirred at  $-78^\circ\text{C}$  for 1 h, warmed and held at  $-30^\circ\text{C}$  for 10 min, and again cooled back to  $-78^\circ\text{C}$ . A suspension of sulfur (465 mg, 14.49 mmol) in 8 mL of dry THF was added dropwise using a 13 gauge needle. Upon addition of the sulfur, the reaction was allowed to stir at  $-78^\circ\text{C}$  for 30 min, and 18% HCl (13 mL) was added in drops. Upon HCl addition, the reaction was allowed to warm slowly to room temperature overnight. The reaction

mixture was extracted with  $3 \times 100 \text{ mL}$  of ether and purified using silica gel column chromatography. A gradient elution beginning with 100% hexanes, 25:1, 15:1, 4:1 hexanes/ether was used to give 2.12 g of the thiol **2** in 73% yield.  $^1\text{H}$  NMR (300 MHz,  $\text{CD}_2\text{Cl}_2$ )  $\delta$  (ppm): 2.37 (s, 3H), 3.42 (s, 1H), 7.24 (d, 2H), 7.33 (d, 2H), 7.46 (d, 4H).  $^{13}\text{C}$  NMR (125 MHz,  $\text{CD}_2\text{Cl}_2$ )  $\delta$  (ppm): 138.27, 137.156, 137.055, 129.387, 129.432, 129.348, 127.261, 126.960, 20.632. GC/MS:  $m/z = 200$ .

**Monolayer Assembly.** All monolayers were assembled according to the standard method described previously.<sup>12</sup> Briefly, the native oxide of GaAs was removed by immersing the substrates in concentrated  $\text{NH}_4\text{OH}$  for 1–5 min. Immediately after immersion, the sample was rinsed with anhydrous ethanol and dried with a  $\text{N}_2$  stream, and SWE measurements were taken within 3 min. The substrates were then immediately immersed in degassed ethanolic solutions containing 3 mM **C<sub>18</sub>** and  $\sim 10 \text{ mM}$   $\text{NH}_4\text{OH}$  and transferred into a nitrogen-purged glove box ( $\text{O}_2 < 5 \text{ ppm}$ ) for incubation for at least 20 h. The samples were removed from solution, dried with  $\text{N}_2$ , and removed from the glovebox for immediate characterization. Once complete analysis was finished for a given sample, the sample was recycled for use by exposure to UV-ozone to remove the monolayer and regrow an oxide layer. The oxide was subsequently removed by etching with  $\text{NH}_4\text{OH}$ . Use of recycled substrates gave results identical to those with fresh substrates. The surface morphologies and surface characteristics of the native oxide and  $\text{NH}_4\text{OH}$  etched substrates were identical to those previously reported.<sup>12,44</sup>

**Contact Angle Measurements.** Sessile drop measurements were made using a home-built apparatus with a CCD camera that captures drop images digitally. The contact angles were analyzed using ImageJ software (National Institute of Health, U.S.A.). A 20- $\mu\text{L}$  drop was dispensed on the surface with a flat-tipped micrometer syringe (GS-1200, Gilmont Instruments, Barrington, IL) for each of the two probe liquids, Milli-Q water and hexadecane (HD). The drop was then pulled at a rate of 50  $\mu\text{m/s}$  across the surface using a piezo-electric micromanipulator to determine the advancing and receding angles. This method has been reported to return an angle somewhere between the max advancing angle and the equilibrium contact angle.<sup>119</sup> A minimum of three measurements were made at different spots for each sample, and at least 3 samples were tested for each probe liquid.

**X-ray Photoelectron Spectroscopy (XPS).** The XPS analyses were performed on a monochromatic Al K $\alpha$  source instrument (Kratos, Axis Ultra; England) operating with a pass energy of 20 eV and an energy step of 0.15 eV. These conditions resulted in a FWHM of 0.71 eV for the Au 4f<sub>7/2</sub> line at 84.0 eV with an average instrumental resolution of  $\sim 0.8 \text{ eV}$ . For internal referencing of C 1s positions, we chose the bulk As 3d<sub>5/2</sub> peak. In all cases, collection times were shorter than the onset of noticeable film degradation determined by comparing survey spectra before and after data collection. Data were collected at a take off angle of  $90^\circ$  from the surface and analyzed using the CASA XPS Analysis program (Neil Farley, Casa XPS). All spectra were referenced to the As 3d<sub>5/2</sub> peak at 40.95 eV.

**Infrared Spectroscopy.** The IR spectra were collected using a custom, in-house modified FTIR spectrometer (BioRad FTS-7000/Digilab, Randolph, MA)<sup>68</sup> with sample-detector optics mounted on a goniometer and housed in an external  $\text{N}_2$  or dry air ( $\text{H}_2\text{O}$ - and  $\text{CO}_2$ -free) purge box. The  $\theta$ – $2\theta$  goniometer allowed continuous selection of angles of incidence from  $\sim 87^\circ$  to  $\sim 20^\circ$  without reconfiguring the optical train. The signal was collected and focused into a liquid  $\text{N}_2$  cooled MCT broad band detector. Spectra were obtained at  $4 \text{ cm}^{-1}$  resolution in order to avoid interference fringes that occur as a result of multiple back reflections (fringing) within the crystal faces of the GaAs wafers. Scans were collected at 20 KHz, and the interferograms were transformed using triangular apodization with zero filling for increased point density where needed. The incident beam was  $p$ -polarized and

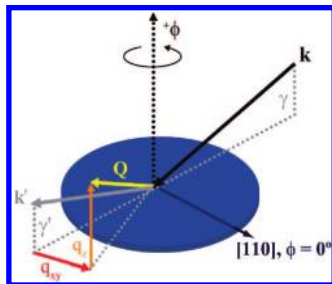


**Figure 11.** Schematic of the scattering geometry in reciprocal space:  $\phi$  = azimuth angle;  $\mathbf{k}$  and  $\mathbf{k}'$  = incident and exit momentum transfer vectors, respectively;  $\mathbf{Q}$  = scattering vector;  $q_{xy}$  and  $q_z$  = in plane and out of plane components of the scattering vector, respectively; and  $\gamma$  and  $\gamma'$  = incident and exit angles, respectively.

set at an 80° angle of incidence (AOI) from the surface normal. Typically ~2000 scans were coadded to improve the signal to noise. For all Au surfaces analyzed, a *p*-polarized incident beam set at an 86° AOI from surface normal was used. Typically the ~800 scans were coadded. Spectral intensities are reported as  $-\log(I/I_0)$ , where  $I$  is the output power of the IR beam from the samples and  $I_0$  is the output power from a reference sample. The most useful reference was a bare GaAs substrate used immediately after oxide removal to minimize contamination. More experimental details have been described previously and can be found in ref 12.

**DFT Calculations.** Optimized geometries and vibrational frequencies of the isolated MBT molecule were determined via Density Functional Theory. The calculations were done using Gaussian 98<sup>120</sup> at the B3LYP/6-31G(d,p) level of theory on a custom-built 10-pc Linux Cluster (Los Alamos Computers, Los Alamos, NM). The initial starting orientation consisted of the molecule in a near-planar configuration with the methyl-phenyl moiety rotated by 5° along the C–C bond to avoid falling into a local minima associated with the fully planar configuration.

**Spectral Simulations.** Simulations of the IRS spectra for the SAMs on GaAs were modeled using a rigorous, full-scale implementation of the 4×4 transfer matrix method developed by Yeh<sup>121</sup> and developed by Parikh and Allara for organic thin film applications.<sup>68</sup> Because GaAs is a semiconducting substrate, the poor conductivity leads to very little screening of the surface components of the electric field, and as a result both parallel and perpendicular components of vibrations of the molecules can be excited.<sup>66</sup> This necessitates determination of all matrix elements of the optical functions. Simulations of the IRS spectra for the SAMs on Au were modeled using a 3×3 transfer matrix method, since only perpendicular components of vibrations of the molecules are excited on metal surfaces.<sup>68</sup>

For reflection measurements using IR-opaque doped GaAs and Au substrates, the SAM structures were modeled as a two-layer planar stack with an optically infinite isotropic substrate and a uniaxially anisotropic SAM (oriented chains with no preferential direction in the surface plane). The GaAs and Au optical function spectra were obtained by interpolating values found from literature.<sup>122</sup> The SAM optical tensor spectra for each selected chain orientation (tilt) were constructed by scaling experimentally obtained isotropic  $k$  spectra of the molecule by the directional cosines of the transition dipole moments of each mode. Spectra were simulated for any chosen SAM thickness, chain tilt, and AOI using codes developed by Parikh and Allara.<sup>68</sup> The calculations yielded reflectivities of the bare substrate ( $R_0$ ) and SAM-covered substrates ( $R$ ). The final absorbance spectra were calculated as  $-\log(R/R_0)$ . A wide variety of model structures were used as inputs to the simulations and the best fit to experimental spectra provided a basis for characterizing the structure of each SAM.

**Grazing Incidence X-ray Diffraction (GIXRD).** Initial attempts to probe for ordering with various modes of AFM (including non-contact (NC) mode under UHV conditions) indicated that clean images are extremely difficult to obtain, even for samples with high organization shown by IRS and wetting. For STM the highest organized films (~2 nm thick) were essentially insulating. Accord-

ingly, GIXRD measurements were carried out. Diffraction patterns were obtained at the G-2 beamline at the Cornell High Energy Synchrotron Source (CHESS) using a 100-mm position-sensitive linear gas detector (Ordel, Inc., Oak Ridge, TN) with a matching large Soller collimator (JJ X-ray, Denmark), which detects exit angle spectra at specific in-plane scattering angles.<sup>123</sup> Each sample was mounted onto a six-circle  $\kappa$  diffractometer<sup>124</sup> and enclosed in a He-purged cylindrical Mylar cell to protect the monolayers from oxidation and to minimize localized X-ray damage. An X-ray wavelength of 1.46 Å was selected using a beryllium single crystal, and the beam was collimated to 1 mm height and 5 mm width, by two sets of slits. The in-plane azimuth direction was calibrated by aligning along the GaAs[220] direction.<sup>125</sup> For the radial scans parallel to the surface, a resolution of  $\Delta q_{xy} = \sim 0.02 \text{ Å}^{-1}$  was used. For azimuth scans, an angular resolution of  $\Delta\phi = 1^\circ$  was used. Each exit angle spectrum took ~60–200 s to collect, depending on the beam intensity. Under these conditions we find that the monolayers are insensitive to X-ray exposure, that is, the integrated X-ray scattering intensity and diffraction positions did not vary within the typical 48 h that each sample was exposed to the X-ray beam. However, post analysis of the samples revealed degradation in the monolayer wetting properties and IRS intensities. All peak positions were determined by fitting the 2D integrated intensity to a Lorentzian line shape.<sup>126</sup> To determine the translational order of the  $\text{C}_{18}$ ,  $\text{C}_{12}$ , and MBT monolayers on the GaAs(001), GIXRD measurements were performed at a grazing angle of  $\gamma = 0.24^\circ$  with respect to the surface plane. This angle is below the critical angle for total external reflection from the GaAs substrate of  $0.3^\circ$ , and in this scattering geometry (see Figure 11), the incident wavevector  $\mathbf{k}$  is essentially in the plane of the surface. The exit wave vector  $\mathbf{k}'$  and thus the scattering vector  $\mathbf{Q}$  have components parallel to the surface and perpendicular to the surface.  $q_{xy}$  characterizes the packing of the alkyl chains, and the  $q_z$  dependence of the scattering provides information about the tilt of the chains.<sup>78</sup>

**Single Wavelength Ellipsometry (SWE).** The SWE measurements were recorded using a Stokes ellipsometer (Gaertner Scientific Corporation, Skokie, IL) set at a 70° angle of incidence and operating at 632.8 nm. The experimentally measured polarization angles were used to determine film thickness using well-established modeling methods.<sup>87,127</sup> The ellipsometric parameters of the bare, freshly etched substrate were measured, and the pseudo-optical constant was calculated. Film thicknesses were calculated using two models. The first used a three isotropic media (air/SAM/substrate) model in which the SAM complex refractive index is described as a real scalar (no loss),  $\hat{n} = n + ik$ ,  $n = 1.47$ , and the substrate is assigned the value measured for the bare substrate just prior to immersion in the thiol solution. The second model used four isotropic layers (air/SAM/interface/substrate) in which substrate optical function values were taken from the literature for an As-terminated GaAs surface<sup>128</sup> and the interface was estimated as a variable-thickness (1–3 Å) As-S layer designed to closely mimic the actual thiolate–GaAs binding interface.<sup>99</sup> The thickness values resulting application of these models to the ellipsometric data, however, consistently deviated significantly from other independent measurements of thickness (see Supporting Information). In particular, the use of the three-medium model led to large sample to sample errors ( $\pm 2 \text{ Å}$ ), which we attribute to the fluctuations of the chemical character of freshly stripped GaAs wafers. We conclude that the simple three-medium model using a freshly cleaned reference is not useful for accurate values. The use of the four-medium model with inclusion of the proper SAM/GaAs interface layer should result in accurate thickness values, and spectroscopic ellipsometry experiments are currently under investigation in our lab to provide reliable interface data.

**Acknowledgment.** The authors acknowledge partial support from the NSF-funded Pennsylvania State University Center for Nanoscale Science (MRSEC Grant DMR-0080019). This work is based in part upon research conducted at the Cornell High Energy Synchrotron Source (CHESS), which is supported by the National Science Foundation under award DMR-0225180.



**Supporting Information Available:** SWE ellipsometry chain length trends; Ga 3d, As 3d, and C 1s XPS spectra; table of C 1s FWHM and peak position values; IR fits for **C<sub>12</sub>**; simulated IRS spectra using the 2 chain per unit cell model; simulated 2 chain per unit cell model IRS spectra with *gauche* defects; GIXRD radial maps of GaAs(001) native oxide and alkanethiolate SAMs [native oxide on GaAs(001), **C<sub>18</sub>** on GaAs(001), **C<sub>12</sub>** on GaAs(001)]; XPS of MBT SAM; optical constants of MBT; simulated isotropic IRS spectra of MBT on GaAs(001) and Au; GIXRD radial maps of MBT SAM. This information is available free of charge via the Internet at <http://pubs.acs.org>.

## REFERENCES AND NOTES

- Ulman, A. Formation and Structure of Self-Assembled Monolayers. *Chem. Rev.* **1996**, *96*, 1533–1554.
- Love, J. C.; Estroff, L. A.; Kriebel, J. K.; Nuzzo, R. G.; Whitesides, G. M. Self-Assembled Monolayers of Thiolates on Metals as a Form of Nanotechnology. *Chem. Rev.* **2005**, *105*, 1103–1169.
- Allara, D. L.; Nuzzo, R. G. Spontaneously Organized Molecular Assemblies. 1. Formation, Dynamics, and Physical Properties of *n*-Alkanic Acids Adsorbed From Solution on an Oxidized Aluminum Surface. *Langmuir* **1985**, *1*, 45–52.
- Schlotter, N. E.; Porter, M. D.; Bright, T. B.; Allara, D. L. Formation and Structure of a Spontaneously Adsorbed Monolayer of Arachidic on Silver. *Chem. Phys. Lett.* **1986**, *132*, 93–98.
- Brzoska, J. B.; Benazouz, I.; Rondelez, F. Silanization of Solid Substrates—A Step toward Reproducibility. *Langmuir* **1994**, *10*, 4367–4373.
- Parikh, A. N.; Allara, D. L.; Azouz, I. B.; Rondelez, F. An Intrinsic Relationship between Molecular-Structure in Self-Assembled *N*-Alkylsiloxane Monolayers and Deposition Temperature. *J. Phys. Chem.* **1994**, *98*, 7577–7590.
- Allara, D. L.; Parikh, A. N.; Rondelez, F. Evidence for a Unique Chain Organization in Long-Chain Silane Monolayers Deposited on 2 Widely Different Solid Substrates. *Langmuir* **1995**, *11*, 2357–2360.
- Nuzzo, R. G.; Zegarski, B. R.; Dubois, L. H. Fundamental Studies of the Chemisorption of Organosulfur Compounds on Au(111). Implications for Molecular Self-Assembly on Gold Surfaces. *J. Am. Chem. Soc.* **1987**, *109*, 733–740.
- Nuzzo, R. G.; Fusco, F. A.; Allara, D. L. Spontaneously Organized Molecular Assemblies. 3. Preparation and Properties of Solution Adsorbed Monolayers of Organic Disulfides on Gold Surfaces. *J. Am. Chem. Soc.* **1987**, *109*, 2358–2368.
- Laibinis, P. E.; Whitesides, G. M.; Allara, D. L.; Tao, Y. T.; Parikh, A. N.; Nuzzo, R. G. Comparison of the Structures and Wetting Properties of Self-Assembled Monolayers of Normal-Alkanethiols on the Coinage Metal-Surfaces, Cu, Ag, Au. *J. Am. Chem. Soc.* **1991**, *113*, 7152–7167.
- Sheen, C. W.; Shi, J. X.; Martensson, J.; Parikh, A. N.; Allara, D. L. A New Class of Organized Self-Assembled Monolayers: Alkane Thiols on GaAs(100). *J. Am. Chem. Soc.* **1992**, *114*, 1514–1515.
- McGuinness, C. L.; Shaporenko, A.; Mars, C. K.; Uppili, S.; Zharnikov, M.; Allara, D. L. Molecular Self-Assembly at Bare Semiconductor Surfaces: Preparation and Characterization of Highly Organized Octadecanethiolate Monolayers on GaAs(001). *J. Am. Chem. Soc.* **2006**, *128*, 5231–5243.
- Porter, M. D.; Bright, T. B.; Allara, D. L.; Chidsey, C. E. D. Spontaneously Organized Molecular Assemblies. 4. Structural Characterization of Normal-Alkyl Thiol Monolayers on Gold by Optical Ellipsometry, Infrared-Spectroscopy, and Electrochemistry. *J. Am. Chem. Soc.* **1987**, *109*, 3559–3568.
- Love, J. C.; Wolfe, D. B.; Haasch, R.; Chabinyc, M. L.; Paul, K. E.; Whitesides, G. M.; Nuzzo, R. G. Formation and Structure of Self-Assembled Monolayers of Alkanethiolates on Palladium. *J. Am. Chem. Soc.* **2003**, *125*, 2597–2609.
- Li, Z. Y.; Chang, S. C.; Williams, R. S. Self-assembly of Alkanethiol Molecules onto Platinum and Platinum Oxide Surfaces. *Langmuir* **2003**, *19*, 6744–6749.
- Lim, H.; Carraro, C.; Maboudian, R.; Pruessner, M. W.; Ghodssi, R. Chemical and Thermal Stability of Alkanethiol and Sulfur Passivated InP(100). *Langmuir* **2004**, *20*, 743–747.
- Schvartzman, M.; Sidorov, V.; Ritter, D.; Paz, Y. Passivation of InP Surfaces of Electronic Devices by Organothiolated Self-Assembled Monolayers. *J. Vac. Sci. Technol., B* **2003**, *21*, 148–155.
- Yamamoto, H.; Butera, R. A.; Gu, Y.; Waldeck, D. H. Characterization of the Surface to Thiol Bonding in Self-Assembled Monolayer Films of C<sub>12</sub>H<sub>25</sub>SH on InP(100) by Angle-Resolved X-ray Photoelectron Spectroscopy. *Langmuir* **1999**, *15*, 8640–8644.
- Gu, Y.; Lin, Z.; Butera, R. A.; Smentkowski, V. S.; Waldeck, D. H. Preparation of Self-Assembled Monolayers on InP. *Langmuir* **1995**, *11*, 1849–1851.
- Tanzer, T. A.; Bohn, P. W.; Roshchin, I. V.; Greene, L. H.; Klem, J. F. Near-Surface Electronic Structure on InAs(100) Modified with Self-Assembled Monolayers of Alkanethiols. *Appl. Phys. Lett.* **1999**, *75*, 2794–2796.
- Dubois, L. H.; Zegarski, B. R.; Nuzzo, R. G. Molecular Ordering of Organosulfur Compounds on Au(111) and Au(100)—Adsorption from Solution and in Ultrahigh Vacuum. *J. Chem. Phys.* **1993**, *98*, 678–688.
- Chidsey, C. E. D.; Liu, G. Y.; Rowntree, P.; Scoles, G. Molecular Order at the Surface of an Organic Monolayer Studied by Low-Energy Helium Diffraction. *J. Chem. Phys.* **1989**, *91*, 4421–4423.
- Alves, C. A.; Smith, E. L.; Porter, M. D. Atomic Scale Imaging of Alkanethiolate Monolayers at Gold Surfaces with Atomic Force Microscopy. *J. Am. Chem. Soc.* **1992**, *114*, 1222–1227.
- Poirier, G. E. Characterization of Organosulfur Molecular Monolayers on Au(111) Using Scanning Tunneling Microscopy. *Chem. Rev.* **1997**, *97*, 1117–1127.
- Camillone, N.; Chidsey, C. E. D.; Liu, G. Y.; Scoles, G. Superlattice Structure at the Surface of a Monolayer of Octadecanethiol Self-Assembled on Au(111). *J. Chem. Phys.* **1993**, *98*, 3503–3511.
- Fenter, P.; Eisenberger, P.; Li, J.; Camillone, N.; Bernasek, S.; Scoles, G.; Ramnarayanan, T. A.; Liang, K. S. Structure of CH<sub>3</sub>(CH<sub>2</sub>)<sub>17</sub>SH Self-Assembled on the Ag(111) Surface: An Incommensurate Monolayer. *Langmuir* **1991**, *7*, 2013–2016.
- Dhirani, A.; Hines, M. A.; Fisher, A. J.; Ismail, O.; Guyot-Sionnest, P. Structure of Self-Assembled Decanethiol on Ag(111): A Molecular Resolution Scanning-Tunneling-Microscopy Study. *Langmuir* **1995**, *11*, 2609–2614.
- Fenter, P.; Eisenberger, P.; Liang, K. S. Chain-Length Dependence of the Structures and Phases of CH<sub>3</sub>(CH<sub>2</sub>)<sub>*n*-1</sub>SH Self-Assembled on Au(111). *Phys. Rev. Lett.* **1993**, *70*, 2447–2450.
- Samant, M. G.; Brown, C. A.; Gordon, J. G. Structure of An Ordered Self-Assembled Monolayer of Docosyl Mercaptan on Gold(111) by Surface X-ray Diffraction. *Langmuir* **1991**, *7*, 437–439.
- Camillone, N.; Eisenberger, P.; Leung, T. Y. B.; Schwartz, P.; Scoles, G.; Poirier, G. E.; Tarlov, M. J. New Monolayer Phases of *n*-Alkane Thiols Self-Assembled on Au(111)—Preparation, Surface Characterization, and Imaging. *J. Chem. Phys.* **1994**, *101*, 11031–11036.
- Poirier, G. E.; Tarlov, M. J. The c(4×2) Superlattice of *n*-Alkanethiol Monolayers Self-Assembled An Au(111). *Langmuir* **1994**, *10*, 2853–2856.
- Poirier, G. E. Coverage-Dependent Phases and Phase Stability of Decanethiol on Au(111). *Langmuir* **1999**, *15*, 1167–1175.
- Tour, J. M. Molecular Electronics. Synthesis and Testing of Components. *Acc. Chem. Res.* **2000**, *33*, 791–804.
- Delamarche, E.; Schmid, H.; Bietsch, A.; Larsen, N. B.; Rothuizen, H.; Michel, B.; Biebuyck, H. Transport Mechanisms of Alkanethiols During Microcontact Printing on Gold. *J. Phys. Chem. B* **1998**, *102*, 3324–3334.
- Kreutz, T. C.; Gwinn, E. G.; Artzi, R.; Naaman, R.; Pizem, H.;



- Sukenik, C. N. Modification of Ferromagnetism in Semiconductors by Molecular Monolayers. *Appl. Phys. Lett.* **2003**, *83*, 4211–4213.
36. Razeghi, M. Optoelectronic Devices Based on III-V Compound Semiconductors Which Have Made a Major Scientific and Technological Impact in the Past 20 Years. *IEEE J. Sel. Top. Quant. Electron.* **2000**, *6*, 1344–1354.
  37. Sze, S. M. *Physics of Semiconductor Devices*; John Wiley and Sons: New York, 1981.
  38. Tsukamoto, S.; Koguchi, N. Observation of Sulfur-Terminated GaAs(001)-(2×6) Reconstruction by Scanning-Tunneling-Microscopy. *Appl. Phys. Lett.* **1994**, *65*, 2199–2201.
  39. Sugiyama, M.; Maeyama, S. Sulfur-Adsorbed GaAs(001) Surface Studied by X-ray Absorption Near Edge Structure, X-ray Standing Waves and X-Ray Diffraction. *Surf. Sci.* **1997**, *385*, L911–L916.
  40. Sugiyama, M.; Maeyama, S.; Oshima, M. Structure of the Sulfur-Passivated GaAs(001) Surface. *Phys. Rev. B* **1994**, *50*, 4905–4908.
  41. Pelzel, R. I.; Nosh, B. Z.; Fimland, B. O.; Weinberg, W. H. Adsorption of [(<sup>t</sup>Bu)GaS]<sub>4</sub> on the GaAs(001)-(4×2) Surface. *Surf. Sci.* **2000**, *470*, L81–L87.
  42. Oigawa, H.; Fan, J. F.; Nannichi, Y.; Ando, K.; Saiki, K.; Koma, A. Studies on an (NH<sub>4</sub>)<sub>2</sub>S<sub>x</sub>-Treated GaAs Surface Using AES, LEELS and RHEED. *Jpn. J. Appl. Phys.* **1989**, *28*, L340–L342.
  43. Oigawa, H.; Fan, J. F.; Nannichi, Y.; Sugahara, H.; Oshima, M. Universal Passivation Effect of (NH<sub>4</sub>)<sub>2</sub>S<sub>x</sub> Treatment on the Surface of III-V Compound Semiconductors. *Jpn. J. Appl. Phys.* **2** **1991**, *30*, L322–L325.
  44. McGuinness, C. L.; Shaporenko, A.; Zharnikov, M.; Walker, A. V.; Allara, D. L. Molecular Self-Assembly at Bare Semiconductor Surfaces: Investigation of the Chemical and Electronic Properties of the Alkanethiolate-GaAs(001) Interface. *J. Phys. Chem. C* **2007**, *111*, 4226–4234.
  45. Jun, Y.; Zhu, X. Y.; Hsu, J. W. P. Formation of Alkanethiol and Alkanedithiol Monolayers on GaAs(001). *Langmuir* **2006**, *22*, 3627–3632.
  46. Nesh, G.; Vilan, A.; Cohen, H.; Cahen, D.; Amy, F.; Chan, C.; Hwang, J. H.; Kahn, A. Energy Level and Band Alignment for GaAs-Alkylthiol Monolayer-Hg Junctions From Electrical Transport and Photoemission Experiments. *J. Phys. Chem. B* **2006**, *110*, 14363–14371.
  47. We note that an incorrect EAL (36 Å) of the Ga 3d electrons through an alkanethiolate SAM was used to calculate the absolute thickness of the alkanethiolate SAMs in this work, in affect decreasing the calculated SAM thickness by ~2 Å from the real value. Furthermore, thicknesses were only calculated from the attenuation of the Ga 3d signals without consideration of the As 3d attenuations.
  48. Nesh, G.; Shpaysman, H.; Cahen, D. Effect of Chemical Bond Type on Electron Transport in GaAs-Chemical Bond-Alkyl/Hg Junctions. *J. Am. Chem. Soc.* **2007**, *129*, 734–735.
  49. Frey, S.; Stadler, V.; Heister, K.; Eck, W.; Zharnikov, M.; Grunze, M.; Zeysing, B.; Terfort, A. Structure of Thioaromatic Self-Assembled Monolayers on Gold and Silver. *Langmuir* **2001**, *17*, 2408–2415.
  50. Leung, T. Y. B.; Schwartz, P.; Scoles, G.; Schreiber, F.; Ulman, A. Structure and Growth of 4-Methyl-4'-mercaptobiphenyl Monolayers on Au(111): A Surface Diffraction Study. *Surf. Sci.* **2000**, *458*, 34–52.
  51. Adlkofer, K.; Shaporenko, A.; Zharnikov, M.; Grunze, M.; Ulman, A.; Tanaka, M. Chemical Engineering of Gallium Arsenide Surfaces with 4'-Methyl-4-mercaptobiphenyl and 4'-Hydroxy-4-mercaptobiphenyl Monolayers. *J. Phys. Chem. B* **2003**, *107*, 11737–11741.
  52. Adlkofer, K.; Eck, W.; Grunze, M.; Tanaka, M. Surface Engineering of Gallium Arsenide with 4-Mercaptobiphenyl Monolayers. *J. Phys. Chem. B* **2003**, *107*, 587–591.
  53. Shaporenko, A.; Adlkofer, K.; Johansson, L. S. O.; Ulman, A.; Grunze, M.; Tanaka, M.; Zharnikov, M. Spectroscopic Characterization of 4'-Substituted Aromatic Self-Assembled Monolayers on GaAs(100) Surface. *J. Phys. Chem. B* **2004**, *108*, 17964–17972.
  54. Shaporenko, A.; Adlkofer, K.; Johansson, L. S. O.; Tanaka, M.; Zharnikov, M. Functionalization of GaAs Surfaces with Aromatic Self-Assembled Monolayers: A Synchrotron-Based Spectroscopic Study. *Langmuir* **2003**, *19*, 4992–4998.
  55. Mars, C. K. *Growth and Characterization of Self-Assembled Molecular Monolayers on Gallium Arsenide*. The Pennsylvania State University, University Park, Pennsylvania, 2000.
  56. Sullivan, P.M.; McGuinness, C.L. Unpublished results.
  57. The **C<sub>1s</sub>** and **C<sub>12</sub>** monolayers have previously been peak fit using high resolution XPS, see ref 44 for detailed fits. Our fits closely match those found for the high resolution method.
  58. Samples were transferred through ambient conditions within 1 min to the XPS analysis chamber. This is equates to the same amount of time the etched samples are exposed to ambient conditions before immersion in the alkanethiol solution.
  59. Heister, K.; Johansson, L. S. O.; Grunze, M.; Zharnikov, M. A Detailed Analysis of the C 1s Photoemission of *n*-Alkanethiolate Films on Noble Metal Substrates. *Surf. Sci.* **2003**, *529*, 36–46.
  60. Biebuyck, H. A.; Bain, C. D.; Whitesides, G. M. Comparison of Organic Monolayers on Polycrystalline Gold Spontaneously Assembled from Solutions Containing Dialkyl Disulfides or Alkenethiols. *Langmuir* **1994**, *10*, 1825–1831.
  61. Zharnikov, M.; Frey, S.; Heister, K.; Grunze, M. Modification of Alkanethiolate Monolayers by Low Energy Electron Irradiation: Dependence on the Substrate Material and on the Length and Isotopic Composition of the Alkyl Chains. *Langmuir* **2000**, *16*, 2697–2705.
  62. These FWHM and BE shifts have been attributed to changes in polarizability of the alkyl chains, which in turn changes their ability to screen the electrostatic interactions between the substrate electrons and the C 1s core hole.<sup>59–61</sup> These effects are not reflective of a change in chemical state of the C atoms. In addition effects such as a decrease in the conformational and orientational order of the molecules have been considered for short alkyl chains.<sup>59–61</sup> Similar FWHM-chain length correlations have also been observed for biphenyl alkyl molecules assembled on Ag and Au.<sup>129</sup>
  63. The theoretical dependence of the C 1s intensity as a function of SAM thickness is given by the equation:

$$I = \int_0^{z_d} \rho_0 e^{-(z/\lambda)} dz$$

where  $z$  = distance into the alkyl chain matrix from the S-C interface towards the vacuum interface,  $z_d$  = the total thickness of the alkyl chain matrix,  $\rho_0$  = intrinsic C 1s photoelectron emission density per unit thickness ( $dI/dz$ ), with no overlayer attenuation, and  $\lambda$  = C 1s photoelectron attenuation length for a fully dense alkyl chain matrix = 35.4 Å.<sup>130</sup> Expressed in terms of a ratio:

$$\begin{aligned} I_n/I_{18} &= \left[ \int_0^{nd_C} \rho_0 e^{-n(d_C/\lambda)} d(nd_C) \right] / \left[ \int_0^{18d_C} \rho_0 e^{-n(d_C/\lambda)} d(nd_C) \right] \\ &= \left[ \int_0^{nd_C} e^{-n\alpha} dn \right] / \left[ \int_0^{18d_C} e^{-n\alpha} dn \right] \\ &= (e^{-n\alpha} - 1) / (e^{-18\alpha} - 1) \end{aligned}$$

where  $d_C$  = thickness of the alkyl matrix per C atom,  $\alpha$  =  $d_C/\lambda$ , and  $n$  = number of C atoms in the alkyl chain but treated as a continuous variable for the integration. With the experimental value of 23.8 (± 0.2) Å for the **C<sub>18</sub>** SAM thickness<sup>12</sup> and correcting for the 1.94 Å S-atom thickness

contribution,<sup>87</sup>  $d_C = [(23.8 - 1.94)/18] = 1.21 \text{ \AA}$  and  $\alpha = 0.0342$  which gives

$$I_n/I_{18} = (e^{-0.0342n} - 1)/(e^{-0.615} - 1) = 2.18 (e^{-0.0342n} - 1)$$

64. If the decrease in monolayer coverage were to result completely in a lower volume density structure (e. g., a void content of  $\sim 13\%$  in the case of the **C<sub>12</sub>** SAM) the corresponding value of  $\lambda$  would increase. Given the established relationship that  $\lambda \propto (\text{density})^{-1/2}$ ,<sup>131</sup> the corrections to the derived surface coverages would be minor, e. g., the void content estimated for the **C<sub>12</sub>** SAM would change from 13% to  $\sim 14\%$ .
65. Petrovykh, D. Y.; Kimura-Suda, H.; Opdahl, A.; Richter, L. J.; Tarlov, M. J.; Whitman, L. J. Alkanethiols on Platinum: Multicomponent Self-Assembled Monolayers. *Langmuir* **2006**, *22*, 2578–2587.
66. The thickness of the each monolayer, used for the IR modeling, was determined from theoretical thicknesses predicted by chain tilt angles determined by NEXAFS<sup>12</sup> and scaled by the length of each *n*-alkanethiol.
67. To achieve a fit within this range of tilt angles, monolayer thicknesses of 10–12 Å were needed, which is significantly thinner than the thickness ( $\sim 14$ –16 Å) predicted from extended all-*trans* chains with this range of chain tilts.
68. Parikh, A. N.; Allara, D. L. Quantitative-Determination of Molecular-Structure in Multilayered Thin-Films of Biaxial and Lower Symmetry from Photon Spectroscopies. 1. Reflection Infrared Vibrational Spectroscopy. *J. Chem. Phys.* **1992**, *96*, 927–945.
69. Because the IRS spectra are the result of an average of all molecular environments, the assumption was made that 50% of the chains had one twist ( $\Psi = 43^\circ$ ) and 50% of the chains had a second twist, rotated  $90^\circ$  ( $\Psi = 133^\circ$ ) to the first. An all-*trans* extended chain was assumed. The specific values of the twist had consequential effects on the fit of the IRS spectra and specifically the ratio of the  $d^-$  and  $d^+$  peak intensities. Thus  $\Psi = 43^\circ$  and  $\Psi = 133^\circ$  were unique answers to the best fit simulation. Using this new model, the subtle difference in the  $r_a^-$  modes observed experimentally was also observed in the simulated spectra; see Supporting Information.
70. Additionally, the effect of *gauche* defects at the terminal methyl group position on the fit of the 2 chain per unit cell model to  $r_a^-$  modes were considered.<sup>10</sup> It was found that introducing up to  $\sim 50\%$  total *gauche* defects (including both *gauche* (1) and *gauche* (2) defects) improved the simulated IRS spectra fit to the experimental data. However, unlike alkanethiolates on Au surfaces, the improvement to the IRS spectral fit is only a subtle effect (see Supporting Information for details).
71. Additional in plane, sharp ( $\Delta q_{xy} \approx 0.01 \text{ \AA}^{-1}$ ) Bragg peaks at  $q_{xy} = 1.39$  and  $1.68 \text{ \AA}^{-1}$  on the **C<sub>18</sub>** SAMs and at  $q_{xy} = 1.29 \text{ \AA}^{-1}$  on the MBT SAMs were also observed from time to time for different monolayer samples. At present their origin is unknown, but given the large difference in  $\Delta q_{xy}$  compared to the main monolayer reflections, these peaks do not appear to be related to the main monolayer structure. Furthermore, these reflections were sometimes observed to have ring-like structures typically associated with powder diffraction pattern from unoriented crystallites. The degree of cleanliness of the samples may be the source of these additional peaks. Most GIXRD experiments of self-assembled monolayers have been conducted under *in situ* vacuum conditions where extensive sputtering, annealing, and heating steps are taken to ensure a clean surface. In contrast, no such steps were taken for these experiments. In one study of alkaneselenolates on Au{111} where the additional cleaning steps were not taken, some of the same spurious peaks were also observed.<sup>75</sup> It has also been observed during these experiments that on one bare native oxide sample that had been reused similar reflections were observed. It should be noted, however, that these peaks were not originally present on a fresh, native oxide surface and result from the monolayer formation process (see Supporting Information).
72. Full radial maps along each direction are included in Supporting Information.
73. The Scherrer equation,  $L = 0.89\lambda/B \cos \theta_B$  where  $\lambda$  is the X-ray wavelength,  $\theta_B$  is the Bragg reflection of the monolayer, and  $B$  is the FWHM of  $\theta_B$ , was used to determined the domain size.
74. A range of domain sizes (90 to  $>1000 \text{ \AA}$ ) have been observed for alkanethiolates on Au surface depending on the preparation conditions. Annealing the surfaces leads to larger domain sizes. See, for example, refs 25, 28, 29, and 133.
75. Samant, M. G.; Brown, C. A.; Gordon, J. G. Formation of an Ordered Self-Assembled Monolayer of Docosaneselenol on Gold(111): Structure by Surface X-Ray Diffraction. *Langmuir* **1992**, *8*, 1615–1618.
76. Samant, M. G.; Brown, C. A.; Gordon, J. G. An Epitaxial Organic Film: The Self-Assembled Monolayer of Docosanoic Acid on Silver(111). *Langmuir* **1993**, *9*, 1082–1085.
77. Kaganer, V. M.; Peterson, I. R.; Kenn, R. M.; Shih, M. C.; Durbin, M.; Dutta, P. Tilted Phases of Fatty-Acid Monolayers. *J. Chem. Phys.* **1995**, *102*, 9412–9422.
78. Kaganer, V. M.; Mohwald, H.; Dutta, P. Structure and Phase Transitions in Langmuir Monolayers. *Rev. Mod. Phys.* **1999**, *71*, 779–819.
79. Ocko, B. M.; Kraack, H.; Pershan, P. S.; Sloutskin, E.; Tamam, L.; Deutsch, M. Crystalline Phases of Alkyl-Thiol Monolayers on Liquid Mercury. *Phys. Rev. Lett.* **2005**, *94*.
80. Tidswell, I. M.; Rabedeau, T. A.; Pershan, P. S.; Kosowsky, S. D.; Folkers, J. P.; Whitesides, G. M. X-Ray Grazing-Incidence Diffraction from Alkylsiloxane Monolayers on Silicon-Wafers. *J. Chem. Phys.* **1991**, *95*, 2854–2861.
81. Xue, Q. K.; Hashizume, T.; Sakurai, T. Scanning Tunneling Microscopy of III-V Compound Semiconductor (001) Surfaces. *Prog. Surf. Sci.* **1997**, *56*, 1–131.
82. Xue, Q. K.; Ling, Y.; Ogino, T.; Sakata, T.; Hasegawa, Y.; Hashizume, T.; Shinohara, H.; Sakurai, T. C<sub>60</sub> Single Crystal Films on GaAs(001) Surfaces. *Thin Solid Films* **1996**, *282*, 618–623.
83. Biegelsen, D. K.; Bringans, R. D.; Northrup, J. E.; Swartz, L. E. Selenium-Terminated and Tellurium-Terminated GaAs(100) Surfaces Observed by Scanning-Tunneling Microscopy. *Phys. Rev. B* **1994**, *49*, 5424–5428.
84. Wang, X.; Hou, X. Y.; Li, Z. S.; Chen, X. Y. X-ray Photoelectron Spectroscopic Studies of Sulphur-Passivated GaAs Surfaces. *Surf. Interface Anal.* **1996**, *24*, 564–568.
85. It is unlikely that a lack of scattering centers due to a decreased chain length is the primary reason for no observation of monolayer reflections for the **C<sub>12</sub>** SAMs. Other GIXRD chain lengths studies of alkanethiols on Au {111} surfaces have observed diffraction from chain lengths as short as nine methylene units. See, for example, refs 28 and 134.
86. Hecht, E. *Optics*, 4th ed.; Addison Wesley: Reading, MA, 2001.
87. Shi, J.; Hong, B.; Parikh, A. N.; Collins, R. W.; Allara, D. L. Optical Characterization of Electronic-Transitions Arising from the Au/S Interface of Self-Assembled *n*-Alkanethiolate Monolayers. *Chem. Phys. Lett.* **1995**, *246*, 90–94.
88. Although the molecular tilt angle can be directly calculated from the ratio of the  $I_{\text{exp}}/I_{\text{iso}}$  of the Z modes, where  $I_{\text{exp}}$  is the experimental intensity and  $I_{\text{iso}}$  is the intensity from the simulated isotropic film of the same thickness as the SAM, attempts to use this method results in deviations in the molecular tilt angle of  $\pm 25^\circ$ . This is most likely due to the fact that approximate dipole moment directions are used in this analysis and were not exclusively oriented along the x, y, or z direction.
89. Krapchetov, D. A.; Ma, H.; Jen, A. K. Y.; Fischer, D. A.; Loo,

- Y. L. Solvent-Dependent Assembly of Terphenyl- and Quaterphenyldithiol on Gold and Gallium Arsenide. *Langmuir* **2005**, *21*, 5887–5893.
90. Nuzzo, R. G.; Korenic, E. M.; Dubois, L. H. Studies of the Temperature-Dependent Phase-Behavior of Long-Chain Normal-Alkyl Thiol Monolayers on Gold. *J. Chem. Phys.* **1990**, *93*, 767–773.
  91. Ungar, G. Structure of Rotator Phases in Normal-Alkanes. *J. Phys. Chem.* **1983**, *87*, 689–695.
  92. Snyder, R. G. Vibrational Spectra of Crystalline *n*-Paraffins. 2. Intermolecular Effects. *J. Mol. Spectrosc.* **1961**, *7*, 116–144.
  93. Kraack, H.; Ocko, B. M.; Pershan, P. S.; Sloutskin, E.; Deutsch, M. Structure of a Langmuir Film on a Liquid Metal Surface. *Science* **2002**, *298*, 1404–1407.
  94. Kraack, H.; Ocko, B. M.; Pershan, P. S.; Sloutskin, E.; Tamam, L.; Deutsch, M. Fatty Acid Langmuir Films on Liquid Mercury: X-ray and Surface Tension Studies. *Langmuir* **2004**, *20*, 5375–5385.
  95. Kraack, H.; Ocko, B. M.; Pershan, P. S.; Sloutskin, E.; Tamam, L.; Deutsch, M. The Structure and Phase Diagram of Langmuir Films of Alcohols on Mercury. *Langmuir* **2004**, *20*, 5386–5395.
  96. Salem, L. Attractive Forces Between Long Saturated Chains at Short Distances. *J. Chem. Phys.* **1962**, *37*, 2100–2113.
  97. Dubois, L. H.; Zegarski, B. R.; Nuzzo, R. G. Fundamental-Studies of Microscopic Wetting on Organic-Surfaces. 2. Interaction of Secondary Adsorbates with Chemically Textured Organic Monolayers. *J. Am. Chem. Soc.* **1990**, *112*, 570–579.
  98. *CRC Handbook of Chemistry and Physics*, 87th ed.; CRC Press: Boca Raton, 2006.
  99. Voznyy, O.; Dubowski, J. J. Structure, Bonding Nature, and Binding Energy of Alkanethiolate on As-Rich GaAs(001) Surface: A Density Functional Theory Study. *J. Phys. Chem. B* **2006**, *110*, 23619–23622.
  100. Vogel, V.; Woll, C. Two-Dimensional Crystal-Structure of Single Langmuir-Blodgett-Films Deposited on Noble-Metal Single-Crystals Studied with LEED. *J. Chem. Phys.* **1986**, *84*, 5200–5204.
  101. It is interesting to note that similar chain driven packing mechanisms have been proposed to explain the ability of long-chain siloxane monolayers to form highly organized assemblies on amorphous SiO<sub>2</sub> and polycrystalline Au substrates.<sup>6,7</sup> In these assemblies the chains are highly conformationally ordered with near vertical tilt angles of ~10°. Further, the assemblies were only highly organized when the substrates were initially activated to allow adsorption of water layers. Accordingly a Langmuir type of assembly at an air–water interface was proposed to explain the substrate independence with the water layer(s) acting to decouple any pinning lattice structure of the substrate from the alkyl chain structure. While pinning lattice geometry restrictions should be unimportant for Au surfaces given the nearly pure dispersion adsorbate–substrate binding forces, they are particularly important for the SiO<sub>2</sub> case where the substrate SiOH (silanol) groups are randomly distributed across the surface and thus direct bonding of the alkylsiloxane groups to this pinning lattice would induce significant chain disorder relative to that observed for the monolayer chain assembly.
  102. This is consistent with the relative reactivities of the four GaAs crystal faces where (110) > (11B) > (001) > (11A).<sup>136,137</sup>
  103. Bareman, J. P.; Cardini, G.; Klein, M. L. Characterization of Structural and Dynamical Behavior in Monolayers of Long-Chain Molecules Using Molecular-Dynamics Calculations. *Phys. Rev. Lett.* **1988**, *60*, 2152–2154.
  104. Schwaha, K.; Spencer, N. D.; Lambert, R. M. Single-Crystal Study of the Initial-Stages of Silver Sulfidation–Chemisorption and Reactivity of Molecular Sulfur (S<sub>2</sub>) on Ag(111). *Surf. Sci.* **1979**, *81*, 273–284.
  105. Tamam, L.; Kraack, H.; Sloutskin, E.; Ocko, B. M.; Pershan, P. S.; Ulman, A.; Deutsch, M. Structure of Mercaptobiphenyl Monolayers on Mercury. *J. Phys. Chem. B* **2005**, *109*, 12534–12543.
  106. Seker, F.; Meeker, K.; Kuech, T. F.; Ellis, A. B. Surface Chemistry of Prototypical Bulk II–VI and III–V Semiconductors and Implications for Chemical Sensing. *Chem. Rev.* **2000**, *100*, 2505–2536.
  107. Bessolov, V. N.; Lebedev, M. V. Chalcogenide passivation of III–V semiconductor surfaces. *Semiconductors* **1998**, *32*, 1141–1156.
  108. Witt, D.; Klajn, R.; Barski, P.; Grzybowski, B. A. Applications Properties and Synthesis of Omega-Functionalized *n*-Alkanethiols and Disulfides—The Building Blocks of Self-Assembled Monolayers. *Curr. Org. Chem.* **2004**, *8*, 1763–1797.
  109. Miyaura, N.; Suzuki, A. Palladium-Catalyzed Cross-Coupling Reactions of Organoboron Compounds. *Chem. Rev.* **1995**, *95*, 2457–2483.
  110. Hassan, J.; Sevignon, M.; Gozzi, C.; Schulz, E.; Lemaire, M. Aryl–Aryl Bond Formation One Century After the Discovery of the Ullmann Reaction. *Chem. Rev.* **2002**, *102*, 1359–1469.
  111. Prim, D.; Campagne, J. M.; Joseph, D.; Andrioletti, B. Palladium-Catalysed Reactions of Aryl Halides with Soft, Non-Organometallic Nucleophiles. *Tetrahedron* **2002**, *58*, 2041–2075.
  112. Miyaura, N. *Advances in Metal–Organic Chemistry*; JAI: London, 1998.
  113. Suzuki, A. *Metal-Catalysed Cross-Coupling Reactions*; Wiley-VCH: New York, 1998.
  114. McLachlan, F.; Mathews, C. J.; Smith, P. J.; Welton, T. Palladium-Catalyzed Suzuki Cross-Coupling Reactions in Ambient Temperature Ionic Liquids: Evidence for the Importance of Palladium Imidazolylidene Complexes. *Organometallics* **2003**, *22*, 5350–5357.
  115. de Boer, B.; Meng, H.; Perepichka, D. F.; Zheng, J.; Frank, M. M.; Chabal, Y. J.; Bao, Z. N. Synthesis and Characterization of Conjugated Mono- and Dithiol Oligomers and Characterization of Their Self-Assembled Monolayers. *Langmuir* **2003**, *19*, 4272–4284.
  116. Skowronskaptasinska, M.; Aarts, V. M. L. J.; Egberink, R. J. M.; Vaneerden, J.; Harkema, S.; Reinhoudt, D. N. Intraannular Functionalization of Macrocyclic Polyethers Via Organo-Lithium Intermediates. *J. Org. Chem.* **1988**, *53*, 5484–5491.
  117. Brzostowska, E. M.; Greer, A. Polysulfane Antitumor Agents From *o*-Benzyne. An Odd–Even Alternation Found in the Stability of Products *o*-C<sub>6</sub>H<sub>4</sub>S<sub>x</sub> (*x* = 1–8). *J. Org. Chem.* **2004**, *69*, 5483–5485.
  118. Sato, R.; Ohyama, T.; Ogawa, S. Efficient Synthesis and Biological Properties of New Benzopentathiepins. *Heterocycles* **1995**, *41*, 893–896.
  119. Bain, C. D.; Troughton, E. B.; Tao, Y. T.; Evall, J.; Whitesides, G. M.; Nuzzo, R. G. Formation of Monolayer Films by the Spontaneous Assembly of Organic Thiols from Solution Onto Gold. *J. Am. Chem. Soc.* **1989**, *111*, 321–335.
  120. Frish, M. J.; Trucks, G. W.; Schlegel, H. B.; Scuseria, G. E.; Robb, M. A.; Cheeseman, J. R.; Zakrzewski, V. G.; Montgomery Jr, J. A.; Stratmann, R. E.; Burant, J. C.; Dapprich, S.; Millam, J. M.; Daniels, A. D.; Kudin, K. N.; Strain, M. C.; Farkas, O.; Tomasi, J.; Barone, V.; Cossi, M.; Cammi, R.; Mennucci, B.; Pomelli, C.; Adamo, C.; Clifford, S.; Ochterski, J.; Petersson, G. A.; Ayala, P. Y.; Cui, Q.; Morokuma, K.; Malick, D. K.; Rabuck, A. D.; Raghavachari, K.; Foresman, J. B.; Cioslowski, J.; Ortiz, J. V.; Baboul, A. G.; Stefanov, B. B.; Liu, G.; Liashenko, A.; Piskorz, P.; Komaromi, I.; Gomperts, R.; Martin, R. L.; Fox, D. J.; Keith, T.; Al-Laham, M. A.; Peng, C. Y.; Nanyakkara, A.; Challacombe, M.; Gill, P. M. W.; Johnson, B.; Chen, W.; Wong, M. W.; Andres, J. L.; Gonzalez, C.; Head-Gordon, M.; Replogle, E. S.; Pople, J. A. *Gaussian 98*, Rev A.9; Gaussian, Inc.: Pittsburgh, PA, 1998.
  121. Yeh, P. *Optical Waves in Layered Media*; Wiley-Interscience: New York, 1988.

122. Palik, E. D. *Handbook of Optical Constants*; Academic Press: New York, 1985.
123. Smilgies, D. M.; Blasini, D. R.; Hotta, S.; Yanagi, H. Reciprocal Space Mapping and Single-Crystal Scattering Rods. *J. Synchrotron Rad.* **2005**, *12*, 807–811.
124. Nowak, D. E.; Blasini, D. R.; Vodnick, A. M.; Blank, B.; Tate, M. W.; Deyhim, A.; Smilgies, D. M.; Abruna, H.; Gruner, S. M.; Baker, S. P. Six-Circle Diffractometer with Atmosphere- and Temperature-Controlled Sample Stage and Area and Line Detectors for Use in the G2 Experimental Station at CHESS. *Rev. Sci. Instrum.* **2006**, *77*.
125. The structure factor for reflections along a direction  $[hkl]$  when  $hkl$  are both odd and even numbers is zero for zinc blende crystals. The structure factor is non-zero when  $hkl$  are all odd or all even with 0 considered even. Therefore, reflections along the  $[100]$  and  $[110]$  direction are not observed.<sup>135</sup> Although measurements were made along the  $[200]$  and  $[220]$  substrate directions, for example, they are referred to as the  $[100]$  and  $[110]$  directions, respectively, to avoid confusion when discussing the unit cell structure.
126. Lorentzian peak shapes have previously been used to determine peak positions diffraction experiments; see ref 132.
127. Collins, R. W.; Kim, Y. T. Ellipsometry for Thin-Film and Surface-Analysis. *Anal. Chem.* **1990**, *62*, A887.
128. Aspnes, D. E.; Studna, A. A. Dielectric Functions and Optical-Parameters of Si, Ge, GaP, GaAs, GaSb, InP, InAs, and InSb from 1.5 to 6.0 eV. *Phys. Rev. B.* **1983**, *27*, 985–1009.
129. Heister, K.; Rong, H. T.; Buck, M.; Zharnikov, M.; Grunze, M.; Johansson, L. S. O. Odd-Even Effects at the S-Metal Interface and in the Aromatic Matrix of Biphenyl-Substituted Alkanethiol Self-Assembled Monolayers. *J. Phys. Chem. B* **2001**, *105*, 6888–6894.
130. Bain, C. D.; Whitesides, G. M. Attenuation Lengths of Photoelectrons in Hydrocarbon Films. *J. Phys. Chem.* **1989**, *93*, 1670–1673.
131. Jablonski, A.; Powell, C. J. Comparisons of Practical Attenuation Lengths Obtained From Different Algorithms for Application in XPS. *Surf. Sci.* **2002**, *520*, 78–96.
132. Barton, S. W.; Thomas, B. N.; Flom, E. B.; Rice, S. A.; Lin, B.; Peng, J. B.; Ketterson, J. B.; Dutta, P. X-ray Diffraction Study of A Langmuir Monolayer of  $C_{21}H_{43}OH$ . *J. Chem. Phys.* **1988**, *89*, 2257–2270.
133. Camillone, N.; Chidsey, C. E. D.; Liu, G.; Scoles, G. Substrate Dependence of the Surface-Structure and Chain Packing of Docosyl Mercaptan Self-Assembled on the (111), (110), and (100) Faces of Single-Crystal Gold. *J. Chem. Phys.* **1993**, *98*, 4234–4245.
134. Fenter, P.; Eberhardt, A.; Liang, K. S.; Eisenberger, P. Epitaxy and Chainlength Dependent Strain in Self-Assembled Monolayers. *J. Chem. Phys.* **1997**, *106*, 1600–1608.
135. Als-Nielsen, J.; McMorrow, D. *Elements of Modern X-Ray Physics*; John Wiley & Sons: New York, 2001.
136. William, R. E. *Gallium Arsenide Processing Techniques*; Artech House, Inc.: Dedham, MA, 1984.
137. Blakemore, J. S. Semiconducting and Other Major Properties of Gallium-Arsenide. *J. Appl. Phys.* **1982**, *53*, R123–R181.